Journal of the Mechanics and Physics of Solids 125 (2019) 89–111

Contents lists available at ScienceDirect

Journal of the Mechanics and Physics of Solids

journal homepage: www.elsevier.com/locate/jmps

A consistently coupled multiscale mechanical–electrochemical battery model with particle interaction and its validation

Bin Wu, Wei Lu*

Department of Mechanical Engineering, University of Michigan, Ann Arbor, MI 48109, USA

ARTICLE INFO

Article history:
Received 21 October 2018
Revised 5 December 2018
Accepted 6 December 2018
Available online 7 December 2018

Keywords:
Electrochemistry
Mechanics
Multiscale
Electrode
Battery

ABSTRACT

As an inherent multiscale structure, a continuum scale battery electrode is composed of many microscale particles. Currently it is generally assumed that each particle is isolated while the stress in a particle only affects solid diffusion. The lack of mechanical interaction between particles and effect of stress on the electrochemical reaction rate makes mechanics and electrochemistry uncoupled at the continuum scale: an applied continuum scale stress in the electrode has no effect on the spatial distribution of electrochemical reaction in the electrode and vice versa. This paper first presents a multiscale model that couples mechanics and electrochemistry consistently at the microscopic and continuum scales. The microscopic particle stress is a superposition of the intra-particle concentration gradient-induced stress and the particle interaction stress, with the latter being related to the continuum scale stress through a representative volume element. The electrochemical charge transfer kinetics is generalized with the stress effect. Diffusion in a particle is described by a chemical potential that includes stress and phase transition. In a parallel effort, we develop a direct three-dimensional particle network model, which consists of realistic active material particles. Unlike the multiscale model, there is no scale separation and homogenization in the particle network model: all particles are modeled explicitly with fully coupled three-dimensional mechanical-electrochemical equations and the finite element method. The results from the particle network model are accurate and can serve as a standard, but the size of particle network that can be calculated is limited due to high computational cost. Comparison of results from the multiscale model and from the particle network model shows that the multiscale model gives good, satisfying accuracy while reducing the computational cost dramatically in comparison to the three-dimensional particle network model. The multiscale model is a power tool to address various coupled problems in the electrode, from inter-particle crack growth to electrode structure design for high performance and long cycle life.

1. Introduction

A lithium-ion battery electrode is an inherent multiscale structure, which consists of many active material particles together with a small amount of binder and conductive additives. An electrode can be considered a continuum since its length scale is generally one or two orders of magnitude larger than the scale of the particles. Therefore, instead of resolving detailed electrode microstructures, the classic pseudo two-dimensional (P2D) electrochemical model (Doyle et al., 1993)

* Corresponding author.
E-mail address: weilu@umich.edu (W. Lu).

https://doi.org/10.1016/j.jmps.2018.12.005
0022-5096/

makes a separation between the electrode scale and the particle scale. The electrode scale is usually one dimensional along the electrode thickness direction, which accounts for solid potential, electrolyte potential and electrolyte concentration. The particle scale provides an additional dimension along the particle radius, which only resolves the solid concentration in the particle. The name of "pseudo two-dimensional" comes from the electrode dimension and the particle dimension, which are spatially separated. The two scales are coupled through the electrochemical kinetics at the particle surface. The P2D porous electrode model is widely used in the field of electrochemistry since it delivers good, satisfying accuracy with acceptable computational cost.

The active materials of lithium-ion battery electrodes exhibit volume change during lithium intercalation or de-intercalation. Owing to the relatively slow rate of solid diffusion, lithium concentration gradient develops inside particles, resulting in inhomogeneous expansion or contraction (Christensen and Newman, 2006). As a result, mechanical stress develops in the particles. The developed stress further affects solid diffusion. The coupled stress and diffusion inside a single particle has been modeled by an analogy to thermal stress (Zhang et al., 2007), which showed that the developed stress can enhance the solid diffusion by 35%. This approach has been extended to study many problems, such as the stress inside a nanowire (Deshpande et al., 2010), a secondary particle consisting of many primary particles (Wu and Lu, 2016), or a particle with an active shell (Wu and Lu, 2017). The effect of active material parameters and morphology on stress has been explored (Purkayastha and McMeeking, 2013; Purkayastha and McMeeking, 2012). Researchers have investigated the fracture of a single particle (Bhandakkar and Gao, 2010, 2011; Zhao et al., 2010) and the stress in active particles with plastic deformation (Zhao et al., 2011; Zhao et al., 2012). Consideration of stress in a single isolated particle extends the classic P2D electrochemical model by giving more accurate solid diffusion in a particle and allowing analysis of particle scale mechanical behaviors such as plasticity and fracture in a particle.

Stress can also affect the reaction kinetics. In a silicon particle coated by carbon shell, the lithiation-induced stress inside the silicon can halt the lithiation process (Jia and Liu, 2016). The stress also affects the lithium deposition rate at the lithium metal surface, which suggests a mechanical approach to suppress the dendrite growth (Monroe and Newman, 2005). In a recent report (Kim et al., 2016), two identical Li-alloyed Si electrodes undergoing asymmetric bending-induced stresses create a difference in the chemical potential, and further generate an electrical current. However, this effect of stress on reaction kinetics has been omitted in most single-particle mechanical models, probably because those models adopt a constant intercalation rate as the boundary condition at the particle surface. Another limitation of the single-particle models is that the stress arising from particle interaction has not been addressed. Studies have shown that inter-particle stress is significant (Xu et al., 2016; Xu and Zhao, 2016). The expansion or contraction of active particles is constrained by neighboring particles, current collectors and the battery case. This constraint can generate stress in a magnitude comparable to concentration gradient-induced stress (Mendoza et al., 2016; Roberts et al., 2014). The lack of mechanical interaction between particles and effect of stress on the electrochemical reaction rate makes mechanics and electrochemistry uncoupled at the continuum scale: an applied continuum scale stress in the electrode has no effect on the spatial distribution of electrochemical reaction in the electrode and vice versa.

The significance of particle interaction is also highlighted by the mechanical failure in the continuum scale, which brings battery degradation. Cracking in-between particles has been well observed in experiments (Liu et al., 2017), which can lead to disruption of electronic network, isolation of active materials, and exposure of fresh surface causing side reactions. In order to consider the cracks in-between particles, a model must include the particle interaction effect. Meanwhile, the intercalation rate at each particle surface is affected by the stress states of different particles. Thus, a model should incorporate the coupling of mechanics and electrochemistry at the continuum electrode scale in addition to the microscopic particle scale.

In this work, we develop two models using different approaches, i.e. a multi-scale model and a direct three-dimensional particle network model. Particle interaction and stress effect on the electrochemical reaction rate are incorporated in both models. We also use a general chemical potential that can capture the effects of both mechanical stress and phase transition on lithium diffusion. The first model couples mechanics and electrochemistry consistently at the microscopic and continuum scales through scale separation and local homogenization. The stress in each microscopic particle is a superposition of the intra-particle concentration gradient-induced stress and the particle interaction stress, and the latter is related to the continuum scale macroscopic stress through a representative volume element (RVE). The second model treats all particles explicitly with fully coupled three-dimensional mechanical-electrochemical equations. The particles and their network structures are simulated directly and accurately without any scale separation or homogenization. By comparing the two models, we demonstrate the unique strength of each model and also use the accurate particle network model to validate the multi-scale model. Comparison of results shows that the multiscale model gives good, satisfying accuracy in simulating coupled mechanical and electrochemical behaviors while reducing the computational cost dramatically in comparison to the particle network model. The limitations of the multi-scale model are also pointed out through the comparison.

By incorporating particle interaction and fully coupling mechanics and electrochemistry consistently from particle to continuum scales, the multi-scale model has provided new physical insights and also serves as a powerful tool to address various coupled problems beyond what can be done currently. For instance, the continuum scale stress at a spatial point is found to directly reflect the average interaction stress for a particle at that point. The inter-particle interaction locally influences lithium intercalation and reaction rate. The continuum scale stress affects the lithium flux distribution in an electrode. As a tool, the multi-scale model enables quantitative investigation of various electrode-level behaviors, such as crack initiation and growth in an electrode, which is a critical problem for battery design. These cracks occur in-between particles

and a model that incorporates particle interaction is essential. The multi-scale model can be further used to investigate how inter-particle cracks lead to the exposure of fresh surface resulting in side reactions, isolation of active particles, and disruption of electronic network. These effects cause capacity fade and an increase of internal resistance. With the multiscale model, the battery electrode is treated as a continuum solid so that existing method for fracture mechanics analysis can be directly applied. It is known that extending fracture mechanics to piezoelectric materials has generated lots of new understanding and interesting results. Similarly, the multiscale model in this paper allows extending fracture mechanics to study electrochemical materials. We expect that exciting new findings and results can be generated. The model can be used to study coupled mechanical-electrochemical degradation behaviors and provide design guidance for increasing the cycle life of a battery. The model will enable the study of new mechanisms and problems not addressed before. For example, imagine a small 'dead' region in an electrode which is electronically isolated from the rest due to poor electronic connection. This region is mechanically the same as the rest, so it is not a crack. This dead region does not participate in lithium intercalation while its surrounding neighbor region does. The expansion of the neighbor region causes stress concentration, reduction of electronic connection, and further growth of the dead region. Such a new type of non-crack damage can be captured only with the proposed fully coupled multiscale model. As another example, the model can be used to study the interesting electrochemical reaction behaviors associated with the stress concentration around a crack tip, or be used to study the self-generated stress and deformation in an electrode for possible actuation applications. As a tool for battery electrode design, the proposed model can be used to design material or electrode patterns to reduce electrode fracture for long battery cycle life, or to design the stress field to facilitate electrochemical reaction and transport for fast charging and other applications beyond what can be done with existing models.

2. Multi-scale model

2.1. Scale separation and coupling

In the electrochemical part, consistent with the porous electrode theory, we separate the microscopic particle scale and the continuum electrode scale. The continuum scale resolves the spatial distribution of solid potential, electrolyte potential and electrolyte lithium concentration in the electrode, while the particle scale resolves the lithium concentration distribution in a particle located at any spatial point in the electrode. Following the widely accepted and validated assumption in electrochemical modeling, we assume spherical particle shape and locally uniform particle size. The condition of locally uniform particle size allows one particle to represent all the particles in its small local region, which corresponds to a spatial point in the continuum scale. Note that in the continuum scale the particle size can be a function of spatial position, so that a distribution of particle sizes can be considered by the model. An example is varying particle sizes along the electrode thickness direction. The essence of multi-scale modeling is that the detail of microstructures becomes insignificant after homogenization, which has been widely used in the mechanical modeling of composites. It should be noted that here our focus is to lay down a framework, which can be extended to consider more general cases such as locally mixed particle sizes or material properties. For instance, if there are two different particle sizes in a local region, we need to consider two representative particles to represent a local region, which corresponds to a spatial point in the continuum scale. This can be done by extending the work in this paper.

In the mechanical part, to address particle interaction, consider a spherical particle in the electrode surrounded by other particles as shown in Fig. 1(a). The stress in particle 1 can be divided into two components. The first component is the intra-particle concentration gradient-induced stress, denoted as σ_{ij}^c. The second component, denoted as σ_{ij}^i, stems from the particle interaction loading, **t**. Note that **t** includes both normal and tangential effects. It should be noted that σ_{ij}^c and σ_{ij}^i affect each other. For instance, particle interaction will regulate the Li concentration in a particle and therefore alter the stress field within the particle. However, such interaction does not mean the two fields are not separable. As will be shown later, the two fields have clear definitions and are uniquely determined without any ambiguity. For instance, σ_{ij}^i is uniquely determined by the force exerted on the particle surface, **t**. σ_{ij}^c is uniquely determined by the concentration field in the particle. Another way to look at the separation of these two fields is to consider it as an approach to facilitate the analytical derivation, since the total stress in a particle is eventually calculated for the electrochemical-mechanical coupling. In this point of view, we do not even require the field separation to be unique, though the two fields are indeed unique and have clear physical meanings.

For a linear elastic problem, the total stress in the particle is a superposition of σ_{ij}^c and σ_{ij}^i. σ_{ij}^c can be easily determined using the intra-particle concentration profile given in the electrochemical part. However, the determination of σ_{ij}^i is more complex because solving the exact **t** exerted on each particle by neighboring particles could be cumbersome. Generally, **t** depends on not only the magnitude of neighboring particle deformation, but also the local morphology of particle network. Our approach is to consider a RVE that consists of many particles as shown in Fig. 1(b), and relate the particle interaction stress to the continuum scale stress, Σ_{ij}, which can be viewed as a far-field load on the RVE.

Based on volume average, the continuum scale stress is given by

$$\Sigma_{ij} = f_s\left\langle \sigma_{ij}^c + \sigma_{ij}^i \right\rangle_s, \tag{1}$$

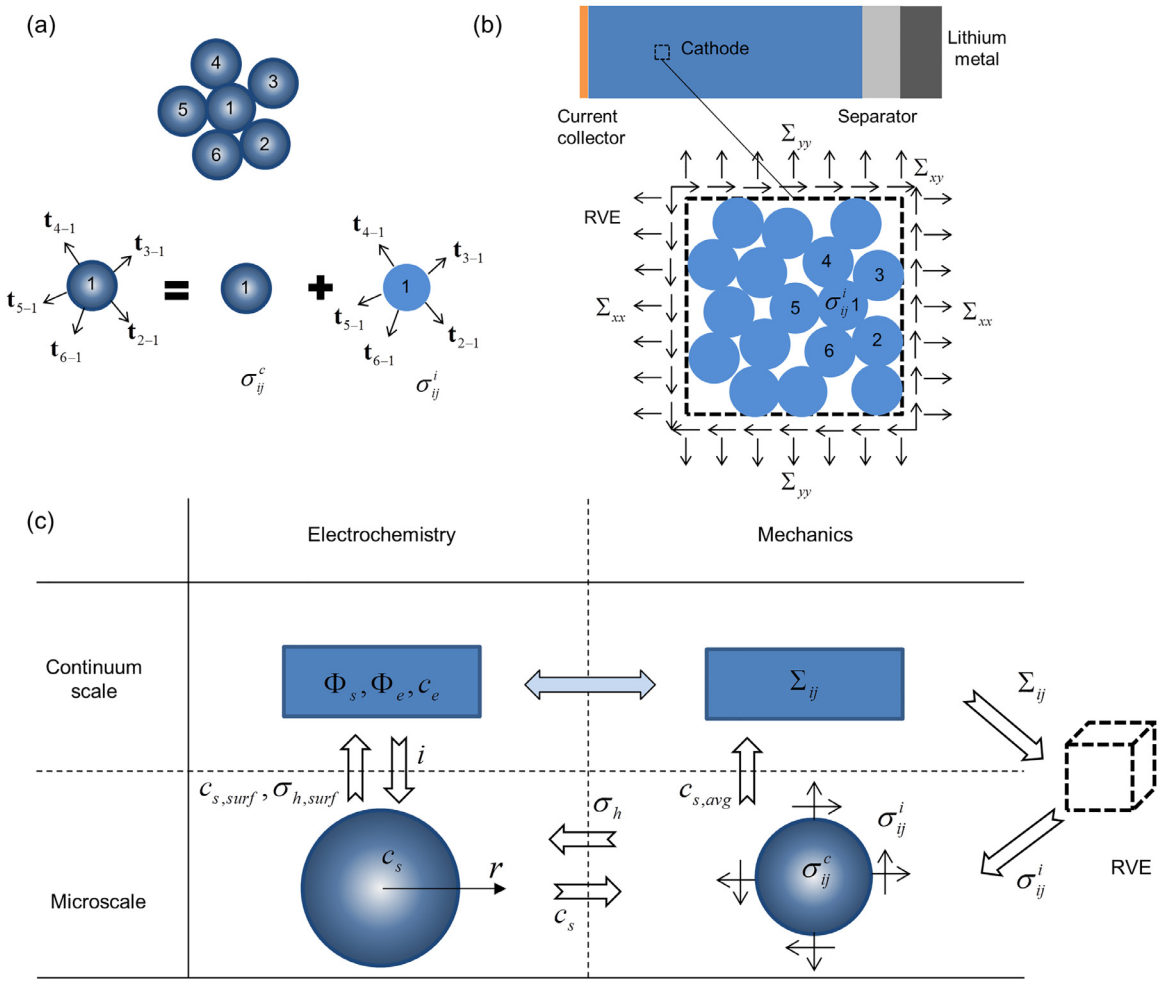

Fig. 1. (a) The stress in a particle is the superposition of the concentration gradient-induced stress, σ_{ij}^{c}, and the stress from particle interaction, σ_{ij}^{i}. (b) The particle interaction stress is related to the continuum scale stress, Σ_{ij}. (c) Schematic of the multi-scale model illustrating the coupling between electrochemistry and mechanics and the coupling between continuum and microscopic scales. Electrochemistry and mechanics are coupled at the microscopic scale through the lithium concentration, c_s, and the hydrostatic stress, σ_h, in the particle, and consistently at the continuum scale through the intercalation reaction current density, i, which depends on the concentration, $c_{s,\,surf}$, and stress, $\sigma_{h,\,surf}$, on the particle surface, and the particle interaction stress, σ_{ij}^{i}, which depends on the average lithium concentration in the particle, $c_{s,\,avg}$.

where $\langle \sigma_{ij}^{c} + \sigma_{ij}^{i} \rangle_s$ is the volume average of stress in the solid and f_s is the volume fraction of the solid. Note that $\langle \sigma_{ij}^{c} \rangle_s = 0$ since the concentration-induced stress in the particle is in a state of self-equilibrium. Thus we have $\Sigma_{ij} = f_s < \sigma_{ij}^{i} >_s$. This equation provides an important insight that the continuum scale stress at a spatial point directly reflects the average interaction stress for a particle at that point.

The average hydrostatic component of the interaction stress is then given by

$$< \sigma_h^i >_s = \frac{\Sigma_{xx} + \Sigma_{yy} + \Sigma_{zz}}{3 f_s}. \tag{2}$$

Fig. 1(c) shows a schematic of the multi-scale model, illustrating the coupling between electrochemistry and mechanics and the coupling between scales. At the microscopic particle scale electrochemistry and mechanics are coupled through (1) the solid lithium concentration in the particle, c_s, which affects the particle stress; and (2) the hydrostatic stress in the particle, σ_h, which affects the solid diffusion. At the continuum scale, the coupling between electrochemistry and mechanics are reflected by the relation between the potential of the solid, Φ_s, the potential of the electrolyte, Φ_e, the lithium ion concentration in the electrolyte, c_e, and the continuum scale stress, Σ_{ij}. The electrochemistry fields Φ_s, Φ_e, c_e and the mechanics fields Σ_{ij} are coupled at the continuum scale in consistency with the microscale coupling through (1) the intercalation reaction current density, i, which at any spatial point in the electrode depends on the concentration, $c_{s,\,surf}$, and stress, $\sigma_{h,\,surf}$, on the surface of a particle located at that point; and (2) the particle interaction stress σ_{ij}^{i} which is affected by the average lithium concentration in the particle, $c_{s,\,avg}$.

2.2. Electrochemistry

2.2.1. Continuum scale

The current density in the electrolyte, $\mathbf{i}_e^H$, the lithium flux density in the electrolyte, $\mathbf{N}_e^H$, and the current density in the solid, $\mathbf{i}_s^H$, are given by

$$\mathbf{i}_e^H = -\kappa_e^H\left[\nabla\Phi_e - \frac{2RT}{F}\left(1+\frac{d\ln f_\pm}{d\ln c_e}\right)(1-t_+)\nabla\ln c_e\right], \tag{3}$$

$$\mathbf{N}_e^H = -D_e^H\nabla c_e + \frac{\mathbf{i}_e^H t_+}{F}, \tag{4}$$

$$\mathbf{i}_s^H = -\kappa_s^H\nabla\Phi_s, \tag{5}$$

where the superscript 'H' denotes continuum locally homogenized quantities. In other words, each spatial point of the electrode represents a local volume containing both the solid phase and the electrolyte solution phase. The flux density per area at a spatial point in the electrode is an average over a local cross-sectional area of the electrode at that spatial point. Take $\mathbf{N}_e^H$ as an example. For a plane with a normal unit vector of $\mathbf{n}$, $\mathbf{n}\cdot\mathbf{N}_e^H$ represents the amount of lithium crossing a unit area of this plane through the solution phase. Note that this density is defined on the unit area referring to the whole cross-sectional area rather than the pore area occupied by the solution phase. This definition is required by the continuum porous electrode theory. In contrast, we define the flux density on the area of each phase in the particle network model in Section 3, where the particles and the electrolyte are modeled explicitly so that they always occupy difference spaces. In that definition the superscript 'H' is removed. In these equations R is ideal gas constant, T is temperature, F is Faraday constant, $f_\pm$ is the electrolyte activity coefficient, and t_+ is the lithium ion transference number.

The homogenized electrolyte conductivity, κ_e^H, solid conductivity, κ_s^H, and electrolyte diffusivity, D_e^H, are given by the Bruggemen relation,

$$\kappa_e^H = \kappa_e f_e^{1.5}, \kappa_s^H = \kappa_s f_s^{1.5}, D_e^H = D_e f_e^{1.5}, \tag{6}$$

where κ_e is the bulk electrolyte conductivity, f_e is the volume fraction of electrolyte, κ_s is the bulk solid conductivity, f_s is the volume fraction of solid, and D_e is the bulk electrolyte diffusivity.

The conservation of charge and mass gives relations to the intercalation reaction current density, i, by

$$\nabla\cdot\mathbf{i}_e^H = a_s i, \tag{7}$$

$$\nabla\cdot\mathbf{i}_s^H = -a_s i, \tag{8}$$

$$f_e\frac{\partial c_e}{\partial t} = -\nabla\cdot\mathbf{N}_e^H + \frac{a_s i}{F}, \tag{9}$$

where the active surface area per unit electrode volume, a_s, is given by

$$a_s = \frac{3f_s}{r_p}, \tag{10}$$

where r_p is the particle radius. The intercalation current density i is given later.

2.2.2. Microscale

The lithium diffusional flux in a solid particle is governed by the gradient of chemical potential (Bohn et al., 2013),

$$\mathbf{N}_s = -Mc_s\nabla\mu, \tag{11}$$

where M is the mobility and μ is the chemical potential of lithium in the solid particles. The diffusion of lithium is associated with the replacement of vacancy with lithium. A rigorous definition of $\mathbf{N}_s$ and μ is given in Appendix A, which has been shown equivalent to this expression.

Under the assumptions of small linear elastic deformation and no dependence of mechanical properties on lithium fraction (Wan and Ciucci, 2017), the chemical potential of lithium in the active particle is given by

$$\mu = \mu_c(c_s) - \Omega\sigma_h, \tag{12}$$

where $\mu_c(c_s)$ denotes the chemical potential at the stress-free state, Ω is the partial molar volume of lithium in the particle, and σ_h is the hydrostatic stress in the particle. Substituting Eq. (12) into Eq. (11), we have

$$\mathbf{N}_s = -Mc_s\left(\frac{\partial\mu_c}{\partial c_s}\nabla c_s - \Omega\nabla\sigma_h\right). \tag{13}$$

The dependence of chemical potential on concentration, $\partial\mu_c/\partial c_s$, can be obtained from the open circuit potential (OCP) curve. The OCP (with respect to lithium metal) of the active particle, E_{ref}, depends on the difference in chemical potential

between a lithium metal (μ_{Li}^0) and the active particle (μ) . When measuring the OCP, the lithium concentration in the particle is uniform, and there is no applied external force. Therefore, the state of battery is stress-free with $\mu = \mu_c(c_s)$. The OCP is given by

$$E_{ref} = \frac{\mu_{\mathrm{Li}}^0 - \mu_c}{F}. \tag{14}$$

The term $\partial\mu_c/\partial c_s$can be determined by the OCP as

$$\frac{\partial \mu_c}{\partial c_s} = -F\frac{\partial E_{ref}}{\partial c_s} = -\frac{F}{c_{s,max}}\frac{\partial E_{ref}}{\partial x_{Li}} = -\frac{FK}{c_{s,max}}, \tag{15}$$

where $c_{s,\,max}$ is the maximum lithium concentration in the solid, x_{Li} is the lithium fraction inside the active material, and $K = \partial E_{ref}/\partial x_{Li}$ is called thermodynamic factor in this work. Note that the thermodynamic factor gives the value corresponding to the stress-free state.

Lithium diffusion in some classic active materials (such as graphite and lithium manganese oxide) occurs by a vacancy mechanism. The mobility decreases with the increase of lithium concentration, which can be written as (Bohn et al., 2013)

$$M = M_0\left(1 - \frac{c_s}{c_{s,max}}\right), \tag{16}$$

where M_0 is the lithium mobility in the solid under the condition of dilute lithium concentration, which relates to the diffusion coefficient by $D_0 = M_0RT$. The diffusion flux in a spherical solid particle is along the radial r direction due to symmetry. With Eqs. (12)–(16), the diffusion flux $N_s(r)$ is given by

$$N_s = \frac{D_0}{RT}\left(\frac{c_s}{c_{s,max}}\right)\left(1 - \frac{c_s}{c_{s,max}}\right)\left(FK\frac{\partial c_s}{\partial r} + \Omega c_{s,max}\frac{\partial \sigma_h}{\partial r}\right). \tag{17}$$

The expression of σ_h is given later.

The diffusion equation is

$$\frac{\partial c_s}{\partial t} + \frac{1}{r^2}\frac{\partial (r^2 N_s)}{\partial r} = 0. \tag{18}$$

The boundary and initial conditions for the solid diffusion are

$$\begin{aligned} \frac{\partial c_s}{\partial r} &= 0 \text{ at } r = 0, \\ N_s &= \frac{i}{F} \text{ at } r = r_p, \\ c_s(r) &= c_{s0} \text{ at } t = 0. \end{aligned} \tag{19}$$

2.2.3. Charge transfer kinetics

Traditionally, the charge transfer kinetics at the solid and electrolyte interface is described using the Butler–Volmer equation,

$$i = i_0\left[\exp\left(\frac{(1-\beta)F\eta}{RT}\right) - \exp\left(-\frac{\beta F\eta}{RT}\right)\right], \tag{20}$$

where i_0 is the exchange current density given by

$$i_0 = Fkc_{s,surf}^{\beta}c_e^{1-\beta}(c_{s,max} - c_{s,surf})^{1-\beta}, \tag{21}$$

where β is the cathodic symmetry factor. In Eq. (20), η is overpotential given by

$$\eta = \Phi_s - \Phi_e - E_{ref}(c_{s,surf}). \tag{22}$$

In this work, the charge transfer kinetics is generalized to include the effect of stress. The detailed derivation can be found in Appendix B. The generalized charge transfer kinetics is given by

$$i = i_0\exp\left[\frac{(\beta_{\mathrm{m}} - \beta)\Omega\sigma_{h,surf}}{RT}\right]\left[\exp\left(\frac{(1-\beta)F\eta_m}{RT}\right) - \exp\left(-\frac{\beta F\eta_m}{RT}\right)\right], \tag{23}$$

where $\sigma_{h,surf} = \sigma_h(r_p)$ is the hydrostatic stress on the particle surface, β_m is the mechanical cathodic symmetry factor, and η_m is the overpotential including the mechanical effect given by

$$\eta_m = \Phi_s - \Phi_e - E_{ref}(c_{s,surf}) - \frac{\Omega\sigma_{h,surf}}{F}. \tag{24}$$

The inclusion of mechanical stress brings two effects: the scaling of exchange current density and the shift of equilibrium potential.

2.3. Mechanics

2.3.1. Continuum scale

The effective elastic modulus of the porous electrode can be determined from those of solid particles using several methods, such as self-consistent method (Hill, 1965), Mori–Tanaka method (Benveniste, 1987; Mori and Tanaka, 1973) and finite element method (Roberts and Garboczi, 2000). In this work, we use the asymptotic homogenization method (Terada et al., 2010; Vel and Goupee, 2010). The details and results of calculation can be found in Appendix C.

The macroscopic stress in the electrode scale, Σ_{ij}, is given by

$$\Sigma_{ij} = C^H_{ijkl}(e_{kl} - e_0\delta_{kl}), \tag{25}$$

where C^H_{ijkl} is the effective elastic modulus and e_{kl} is the strain. The eigenstrain of a RVE, $e_0\delta_{kl}$, comes from its volumetric change associated with the lithium intercalation/deintercalation of its particles. Here δ_{ij} is the Kronecker delta. e_0 is determined by the average concentration of the particle, $c_{s,\,avg}$, and the initial concentration, c_{s0}, giving

$$e_0 = \frac{\Omega^H}{3}(c_{s,avg} - c_{s0}), \tag{26}$$

where the "effective" partial molar volume of RVE, Ω^H, may differ from the Ω in Eq. (12) since only the active particles in the porous RVE are associated with the intercalation-induced strain. The relation between Ω^H and Ω is analogously to the relation between the thermal expansion coefficient of a porous solid and a bulk solid. In this work the "effective" Ω^H is calculated using the asymptotic homogenization method shown in Appendix C, which yields $\Omega^H = \Omega$.

The equilibrium of macroscopic stress gives

$$\nabla \cdot \mathbf{\Sigma} = \mathbf{0}. \tag{27}$$

2.3.2. Microscale

In this section, we focus on the calculation of σ_h in a particle. Here we consider the average interaction stress of a particle because of interaction with all its neighbors. The hydrostatic stress on the particle surface is given by $\sigma_{h,surf} = \sigma^c_h(r_p) + < \sigma^i_h >_s$. Eq. (2) has already related $< \sigma^i_h >_s$ to the macroscopic stress. So here we focus on σ^c_h, the concentration-induced stress in an isolated particle.

The radial strain, ε^c_{rr}, and the tangential strain, $\varepsilon^c_{\theta\theta}$, are given by the radial displacement, u,

$$\varepsilon^c_{rr} = \frac{du}{dr},\ \varepsilon^c_{\theta\theta} = \frac{u}{r}. \tag{28}$$

The strains include an elastic part and a lithiation-induced part that is analogous to thermal strain,

$$\begin{aligned}
\varepsilon^c_{rr} &= \frac{1}{E_p}\left(\sigma^c_{rr} - 2\nu_p\sigma^c_{\theta\theta}\right) + \frac{\Omega}{3}\tilde{c},\\
\varepsilon^c_{\theta\theta} &= \frac{1}{E_p}\left(\sigma^c_{\theta\theta} - \nu_p\left(\sigma^c_{\theta\theta} + \sigma^c_{rr}\right)\right) + \frac{\Omega}{3}\tilde{c},
\end{aligned} \tag{29}$$

where $\tilde{c} = c_s - c_{s0}$ is the difference between lithium concentration at the current state, c_s, and the initial stress-free state, c_{s0}. E_p is the Young's modulus of the particle, ν_p is the Poisson's ratio of the particle, σ_{rr} is the radial stress, and $\sigma_{\theta\theta}$ is the tangential stress.

The equilibrium equation is given by

$$\frac{d\sigma^c_{rr}}{dr} + \frac{2}{r}\left(\sigma^c_{rr} - \sigma^c_{\theta\theta}\right) = 0. \tag{30}$$

The boundary conditions are

$$\begin{aligned}
&u = 0 \text{ at } r = 0,\\
&\sigma^c_{rr} = 0 \text{ at } r = r_p.
\end{aligned} \tag{31}$$

Solving Eqs. (28)–(31), we get

$$\sigma^c_{rr}(r) = \frac{2\Omega E_p}{3(1-\nu_p)}\left(\frac{1}{r_p^3}\int_0^{r_p}\tilde{c}r^2dr - \frac{1}{r^3}\int_0^{r}\tilde{c}r^2dr\right), \tag{32}$$

$$\sigma^c_{\theta\theta}(r) = \frac{\Omega E_p}{3(1-\nu_p)}\left(\frac{2}{r_p^3}\int_0^{r_p}\tilde{c}r^2dr + \frac{1}{r^3}\int_0^{r}\tilde{c}r^2dr - \tilde{c}\right). \tag{33}$$

$$\sigma^c_h(r) = \frac{\sigma^c_{rr} + 2\sigma^c_{\theta\theta}}{3} = \frac{2\Omega E_p}{3(1-\nu_p)}\left(\frac{1}{r_p^3}\int_0^{r_p}\tilde{c}r^2dr - \frac{\tilde{c}}{3}\right). \tag{34}$$

Eq. (34) shows that $\sigma_h^c(r)$ is determined by the concentration profile in the particle and can be obtained by an integration. $\sigma_h^c(r_p)$ is given by evaluating $\sigma_h^c(r)$ at $r = r_p$. We can also get the radial displacement at the particle surface,

$$u^c(r_p) = \frac{\Omega}{r_p^2}\int_0^{r_p} \tilde{c} r^2 dr = \frac{\Omega r_p}{3}(c_{s,avg} - c_{s0}), \tag{35}$$

where $c_{s,avg} = (3/r_p^3)\int_0^{r_p} c_s(r) r^2 dr$ is the average lithium concentration inside the particle. Eq. (35) shows that the overall expansion or contraction of a particle, $u^c(r_p)/r_p = (\Omega/3)(c_{s,avg} - c_{s0})$, only depends on the average concentration regardless of the concentration profile. This result provides the basis of using the average concentration in Eq. (26).

3. Direct three-dimensional particle network model

In this model we consider all particles and their network structure explicitly with fully coupled three-dimensional mechanical-electrochemical equations.

The ionic current inside the electrolyte is described by

$$\mathbf{i}_e = -\kappa_e\left[\nabla\Phi_e - \frac{2RT}{F}\left(1 + \frac{d\ln f_{\pm}}{d\ln c_e}\right)(1 - t_+)\nabla \ln c_e\right], \tag{36}$$

where κ_e is the electrolyte conductivity. Note that although the form of Eq. (36) appears similar as Eq. (3), a major difference is that here the current density per area, $\mathbf{i}_e$, is defined on the cross-sectional area of a single phase instead of on the cross-sectional area of local phase mixtures, so κ_e instead of κ_e^H appears in the equation. Also note that in giving Eq. (36), Φ_e is defined as the potential of a lithium metal reference electrode at the point of interest in the electrolyte with respect to another lithium metal reference electrode at a fixed point (see more discussion on the definition of electrolyte potential in Section 12.4 of (Newman, 1991)).

The lithium ion flux inside the electrolyte is driven by diffusion and migration,

$$\mathbf{N}_e = -D_e\nabla c_e + \frac{\mathbf{i}_e t_+}{F}, \tag{37}$$

where D_e is lithium ion diffusivity in the electrolyte.

The current in the solid particle matrix is given by

$$\mathbf{i}_s = -\kappa_s\nabla\Phi_s, \tag{38}$$

where κ_s is solid conductivity.

Similar as Eq. (17) but using the general gradient operator, the lithium flux in solid is given by

$$\mathbf{N}_s = \frac{D_0}{RT}\left(\frac{c_s}{c_{s,max}}\right)\left(1 - \frac{c_s}{c_{s,max}}\right)(FK\nabla c_s + \Omega c_{s,max}\nabla\sigma_h). \tag{39}$$

Note that a particle is no longer spherically symmetric with explicit modeling of the particle network, therefore a general gradient operator is used.

The conservation of mass requires

$$\frac{\partial c_e}{\partial t} + \nabla\cdot\mathbf{N}_e = 0, \tag{40}$$

$$\frac{\partial c_s}{\partial t} + \nabla\cdot\mathbf{N}_s = 0. \tag{41}$$

The conservation of charge requires

$$\nabla\cdot\mathbf{i}_e = 0, \tag{42}$$

$$\nabla\cdot\mathbf{i}_s = 0. \tag{43}$$

The charge transfer kinetics at the particle surface follows Eq. (23), with the exchange current density given by Eq. (21) and the generalized overpotential given by Eq. (24).

Using the charge transfer current at the electrolyte-particle interface, the boundary conditions for $\mathbf{N}_e$, $\mathbf{N}_s$, $\mathbf{i}_e$ and $\mathbf{i}_s$ are

$$\begin{aligned}
\mathbf{n}\cdot\mathbf{N}_e &= \frac{i}{F},\\
\mathbf{n}\cdot\mathbf{N}_s &= \frac{i}{F},\\
\mathbf{n}\cdot\mathbf{i}_e &= i,\\
\mathbf{n}\cdot\mathbf{i}_s &= i.
\end{aligned} \tag{44}$$

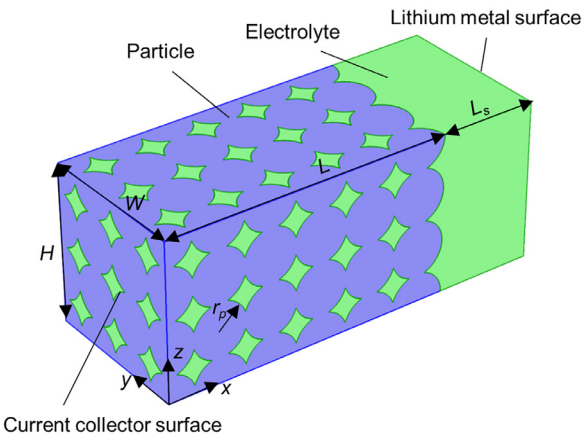

Fig. 2. Schematic of the three-dimensional particle network model. r_p denotes the particle radius, L denotes the electrode thickness, H denotes the electrode height, Wdenotes the electrode width and L_s denotes the separator thickness. The distance between the centers of two neighboring particles is $1.9r_p$. (For interpretation of the references to color in this figure, the reader is referred to the web version of this article.)

where $\mathbf{n}$ is the unit normal vector pointing from the solid particle to the electrolyte.

The particle network forms a continuum solid of complicated geometry. The stress is the solid is given by

$$\sigma_{ij} = C_{ijkl}(e_{kl} - e_0\delta_{kl}), \tag{45}$$

where $C_{ijkl} = \lambda\delta_{ij}\delta_{kl} + \mu(\delta_{ik}\delta_{jl} + \delta_{il}\delta_{jk})$ is the elastic modulus, $\lambda = E\nu/[(1+\nu)(1-2\nu)]$ and $\mu = E/[2(1+\nu)]$. The eigen-strain at each spatial point in the solid is

$$e_0 = \frac{\Omega}{3}(c_s - c_{s0}), \tag{46}$$

where c_{s0} is the initial lithium concentration of the solid at the stress-free state.

The equilibrium of stress is given by

$$\nabla \cdot \boldsymbol{\sigma} = \mathbf{0}. \tag{47}$$

4. Examples

In the following we layout the detailed boundary and initial conditions using specific examples. For comparison, we will calculate the same setup using both the multiscale model and the particle network model. To introduce the setup we start with the particle network model since it provides more microstructure details.

4.1. Direct simulation with three-dimensional particle network model

Fig. 2 shows the schematic of the three-dimensional particle network model. The overlapping active particles constitute the backbone of the electrode, while the porous volume in-between the particles is occupied by the electrolyte. Binder, carbon black and other additives are omitted in the geometry. Lithium metal serves as the counter electrode. In application, there is a separator sandwiched between the electrode and lithium metal to avoid internal short-circuit. With a focus on modeling the electrode and the separator is very compliant, here we use a space to represent the separator.

The symmetrical boundary conditions hold for $\mathbf{N}_e$, $\mathbf{N}_s$, $\mathbf{i}_e$ and $\mathbf{i}_s$ at the boundaries of $y = 0$, $y = W$, $z = 0$ and $z = H$, which are given by

$$\begin{aligned} &\mathbf{n}\cdot\mathbf{N}_e = 0, \mathbf{n}\cdot\mathbf{N}_s = 0, \\ &\mathbf{n}\cdot\mathbf{i}_e = 0, \mathbf{n}\cdot\mathbf{i}_s = 0. \end{aligned} \tag{48}$$

where $\mathbf{n}$ is the unit normal vector pointing outside from the model domain.

At $x = 0$, where particles or electrolyte meet the current collector, we have

$$\begin{aligned} &\mathbf{n}\cdot\mathbf{N}_e = 0, \mathbf{n}\cdot\mathbf{N}_s = 0, \\ &\mathbf{n}\cdot\mathbf{i}_e = 0, \mathbf{n}\cdot\mathbf{i}_s = -i_{app}. \end{aligned} \tag{49}$$

where $\mathbf{n}$ is the unit normal vector pointing from the current collector to the electrode, i_{app} is the applied current density and $i_{app} > 0$ for discharge (lithium ions move from lithium metal to the electrode).

The boundary conditions at the lithium metal surface, $x = L + L_s$, are given by

$$\mathbf{n}\cdot\mathbf{N}_e = -\frac{i_{app}}{F}, \mathbf{n}\cdot\mathbf{i}_e = -i_{app}. \tag{50}$$

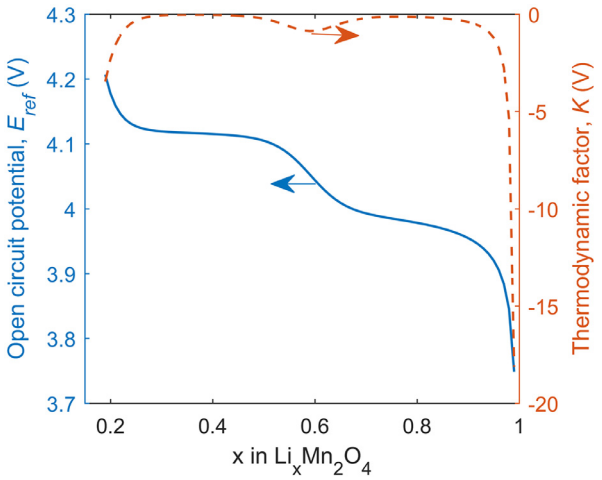

Fig. 3. Open circuit potential and thermodynamic factor profiles of $Li_xMn_2O_4$.

where $\mathbf{n}$ is the unit normal vector pointing from the electrolyte to lithium metal.

The initial conditions are given by

$$c_e = c_{e0}, c_s = c_{s0} \text{ at } t = 0. \tag{51}$$

The mechanical boundary conditions are given by

$$\begin{aligned} \mathbf{u} &= \mathbf{0} \text{ at } x = 0, \\ \mathbf{n}\cdot\mathbf{u} &= 0 \text{ at } y = 0, y = W, z = 0, z = H, \\ \mathbf{n}\cdot\boldsymbol{\sigma} &= \mathbf{0} \text{ at particle electrolyte interface.} \end{aligned} \tag{52}$$

where $\mathbf{u}$ is displacement, $\mathbf{n}$ is the unit normal vector pointing outside from the model domain in the expression of $\mathbf{n}\cdot\mathbf{u} = 0$, and $\mathbf{n}$ is the unit normal vector pointing from the particle to the electrolyte at the particle electrolyte interface in the expression of $\mathbf{n}\cdot\boldsymbol{\sigma} = \mathbf{0}$.

4.2. Multi-scale model

Now we solve the same setup in Fig. 2 using the multi-scale model. Note that at the continuum scale the problem is essentially one dimensional in the x axis because of symmetry in the y and z axes. The fluxes $\mathbf{i}_e^H$, $\mathbf{N}_e^H$, and $\mathbf{i}_s^H$ are all along the x axis, or the electrode thickness direction. Therefore, in the following we remove the vector form for conciseness. The boundary and initial conditions are given by

$$\begin{aligned} i_s^H &= -i_{app}, i_e^H = 0, N_e^H = 0 \text{ at } x = 0, \\ i_s^H &= 0, i_e^H = -i_{app} \text{ at } x = L, \\ \Phi_s &= 0, i_e^H = -i_{app}, N_e^H = -\frac{i_{app}}{F} \text{ at } x = L + L_s, \\ c_e(x) &= c_{e0} \text{ at } t = 0. \end{aligned} \tag{53}$$

The mechanical boundary conditions are given by

$$\begin{aligned} u_x = u_y = u_z &= 0 \text{ at } x = 0, \\ \Sigma_{xx} = \Sigma_{xy} = \Sigma_{xz} &= 0 \text{ at } x = L, \\ u_y &= 0 \text{ at } y = 0 \text{ and } y = W, \\ u_z &= 0 \text{ at } z = 0 \text{ and } z = H. \end{aligned} \tag{54}$$

4.3. Parameters

In this work we choose $Li_xMn_2O_4$ as the cathode for two reasons. First, as a well studied material, the chemical and mechanical properties of $Li_xMn_2O_4$ are available in the literature. Second, the lithiation of $Li_xMn_2O_4$ is associated with phase transition, which can demonstrate the capability of the generalized solid diffusion equation to capture this phase transition effect. The open circuit potential and the thermodynamic factor of $Li_xMn_2O_4$ are given in Fig. 3.

Table 1
Input parameters for the two models.

Parameter	Symbol	Value
Microscale		
Particle radius	r_p	5 μm
Diffusivity of lithium ions in solid	D_0	1×10^{-14} m^2 s^{-1}
Reaction rate constant (Dai et al., 2014)	k	5×10^{-10} m$^{2.5}$ mol$^{-0.5}$ s^{-1}
Maximum lithium concentration in solid (Dai et al., 2014)	$c_{s,\,max}$	24161 mol m^{-3}
Initial lithium concentration in solid (Dai et al., 2014)	c_{s0}	$0.19c_{s,\,max}$
Young's modulus of the solid particle (Zhang et al., 2007)	E_p	10 GPa
Poisson's ratio of the solid particle (Zhang et al., 2007)	ν_p	0.3
Lithium ion partial molar volume (Zhang et al., 2007)	Ω	3.497×10^{-6} m^3 mol^{-1}
Continuum scale		
Cathode thickness	L	52.5 μm
Cathode width	W	28.5 μm
Cathode height	H	28.5 μm
Separator thickness	L_s	17.5 μm
Initial lithium ion concentration in electrolyte	c_{e0}	1000 mol m^{-3}
Cathode porosity	f_e	0.40
Volume fraction of active material	f_s	0.60
Lithium ion transference number	t_+	0.38
Solid electronic conductivity (Dai et al., 2014)	κ_s	10 S m^{-1}
Electrolyte conductivity (Dai et al., 2014)	κ_e	1 S m^{-1}
Diffusivity of lithium ions in bulk electrolyte (Dai et al., 2014)	D_e	3.23×10^{-10} m^2 s^{-1}
Temperature	T	298 K
Activity coefficient term	$1 + \frac{d \ln f_{\pm}}{d \ln c_e}$	2.83
Cathodic symmetry factor	β	0.5
Mechanical cathodic symmetry factor	β_m	0.5

Table 1 lists the input parameters for the two models. Note that different literatures may give quite different values of material parameters depending on the measurement techniques they used. Our focus is to demonstrate how the framework works so the discrepancy among measured material parameters in the literature is not of concern. Here we choose values of material parameters that have been widely used before. With the same inputs, we compare the predictions from the two models.

For the direct three-dimensional particle network model the applied current density is $i_{app} = 64$ A m^{-2}, which is typical for a $LiMn_2O_4$ electrode in automotive applications. Note that this current density is defined based on the cross-sectional area of the solid phase, i.e. the total cross-sectional area of all the particles that meet the current collector (the blue area in the y–z plane at $x = 0$ in Fig. 2). For the multiscale model, we keep the same amount of current passing through the electrode so that the results are comparable. Since the current density of the multiscale model is defined on the apparent cross-sectional area of the electrode, the corresponding applied current density is smaller, and the calculation gives $i_{app} = 54.2$ A m^{-2} for the multiscale model.

The direct multiscale model and the three-dimensional particle network model are both solved using finite element software package COMSOL Multiphysics. In terms of computational cost, the three-dimensional model takes more than 9 h on a workstation while the multiscale model takes less than 1 h on the same workstation.

5. Results and discussion

5.1. Simulation results from multi-scale model

Fig. 3(a) shows the distribution of lithium concentration inside particles at different positions along the electrode thickness. The phase transition-induced concentration jump vanishes in particles closer to the separator ($x/L = 1$), while still exists in particles closer to the current collector ($x/L = 0$). The concentration gradient-induced stresses are shown in Fig. 3(b) and (c). The particles with concentration jump exhibit significantly larger radial and tangential stresses. This result highlights the importance to include the phase transition effect into solid diffusion, otherwise the calculated stress will be significantly underestimated. Fig. 4(d) shows the macroscopic stress in the electrode. Note that $\Sigma_{xx} = 0$ since the electrode is free to expand in the x direction. Particles near the separator shows larger compressive stresses of Σ_{yy} and Σ_{zz} because more lithium ions intercalate into those particles.

In terms of temporal profiles, we choose one particle at the location of $x/L = 0.36$. As shown in Fig. 5(a), the radial and tangential stress at the particle center ($\sigma^c_{rr}(r = 0), \sigma^c_{\theta\theta}(r = 0)$) peak at the time of about 500 s, while the tangential stress at the particle surface ($\sigma^c_{\theta\theta}(r = r_p)$) reaches its maximum magnitude at about 200 s. This time lag corresponds to the radial inward movement of the concentration jump. In contrast, Fig. 5(b) shows that the continuum scale stress is compressive and its magnitude gradually increases with time, as the increasing lithium concentration in the solid results in larger and larger expansion.

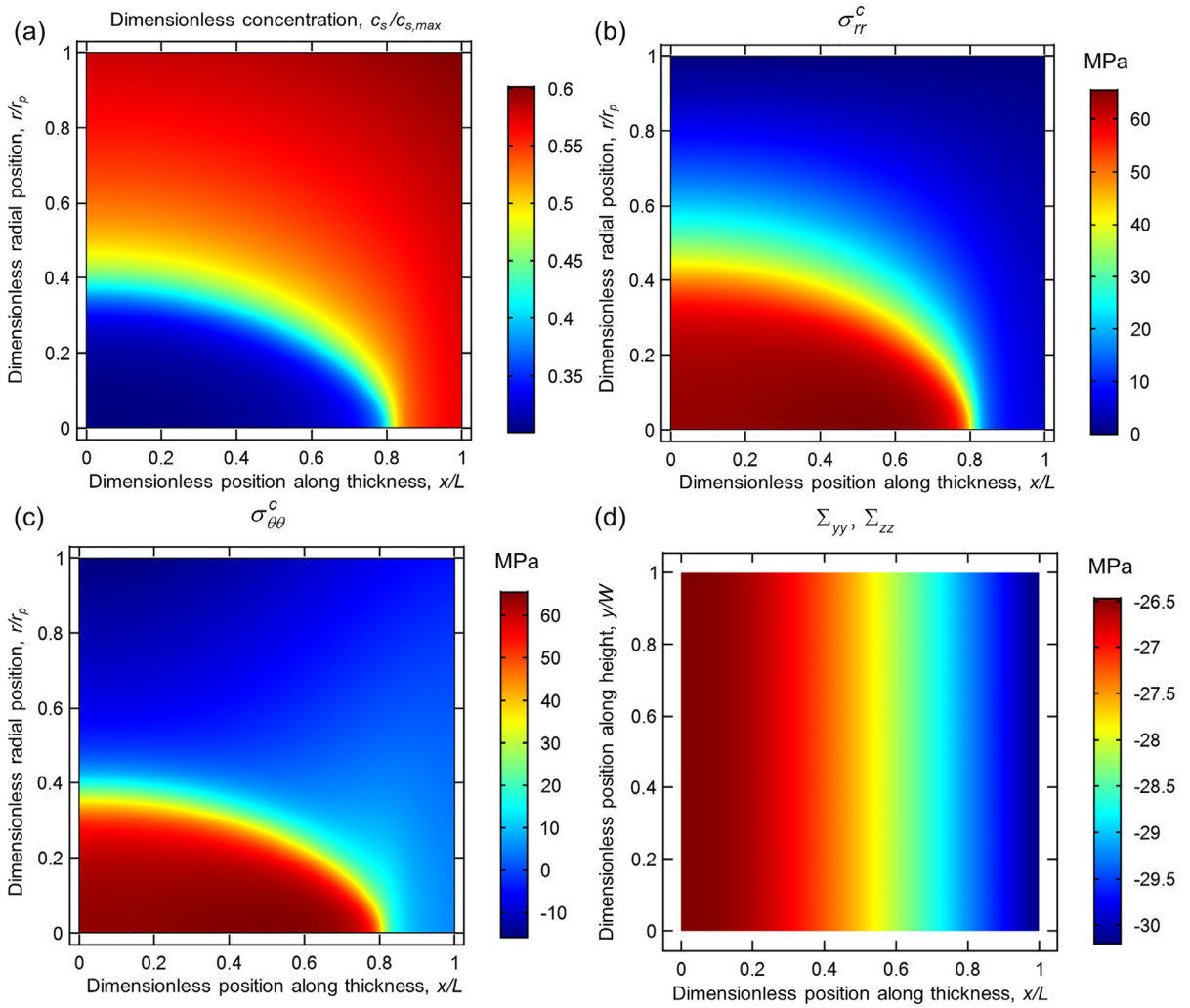

Fig. 4. Distribution of (a) lithium concentration, (b) radial stress, and (c) tangential stress along particle radius inside all particles. In (a)–(c), the horizontal axis represents particle location along the electrode thickness direction and the vertical axis represents a point in the particle. (d) Distribution of macroscopic stress inside the electrode, where the horizontal axis represents the location along the thickness direction and the vertical axis represents the location along the width direction. All results shown are at the instant of 500 s.

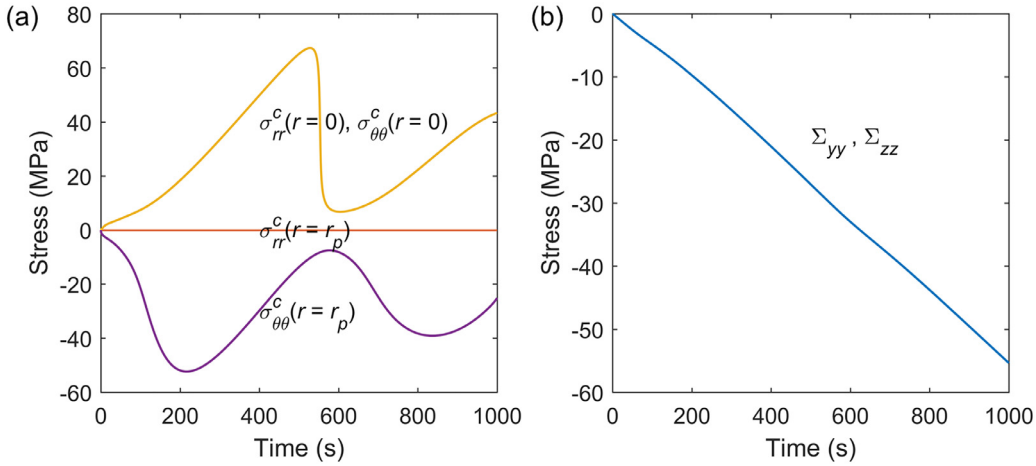

Fig. 5. Temporal profiles of (a) concentration gradient-induced stress in a microscale particle and (b) continuum electrode scale stress at the location of $x/L = 0.36$.

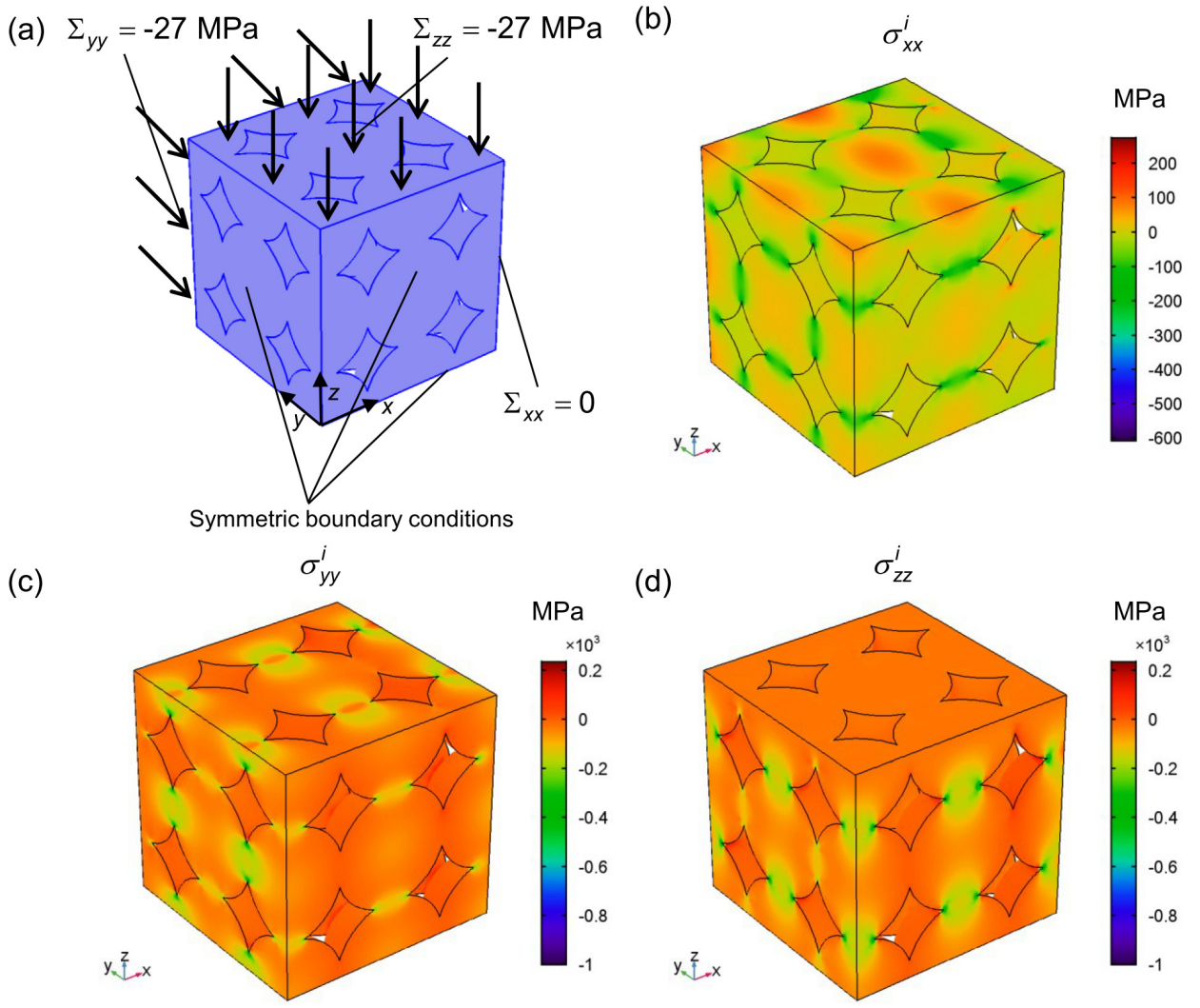

Fig. 6. (a) Schematic of the RVE and the boundary conditions. Distribution of (b) σ^i_{xx}, (c) σ^i_{yy} and (d) σ^i_{zz} inside a RVE.

Fig. 6 shows the distribution of interaction stress inside a local RVE. This is obtained by modeling the local detailed particle structure in the RVE with finite element and applying the solved continuum scale stress as boundary loads. The particles have a uniform lithium concentration so there is no lithium concentration gradient-induced stress, and the stress comes purely from contact. Large stress concentration shows up naturally at the contact between particles. This indicates that the detailed contact-induced local inhomogeneous stress distribution at any spatial point of interest in the electrode, if needed, can be recovered by using the solved continuum scale stress and a RVE.

5.2. Simulation results from direct particle network model

Fig. 7(a) shows the lithium concentration distribution at the instant of 500 s. A sharp concentration jump is observed to form inside most particles, except for those near the separator. This concentration jump results from the phase transition of $Li_xMn_2O_4$ during $0.25 < x < 0.5$, which corresponds to the OCP plateau of 4.15 V shown in Fig. 3. With lithium intercalation, the concentration jump gradually moves towards particle center until vanishes. The radial locations of concentration jump at different particles thus represent the history of intercalation current: the particles near the separator with a larger intercalation rate has finished the phase transition, while the particles near the current collector still have a moving concentration jump. Another observation is that the concentration is almost spherically symmetrical, thus the assumption of radial diffusion in the multi-scale model is reasonable.

Note that the stresses in Fig. 7(b)–(d) result from both concentration gradient in the particles and from particle interactions. At the particle center, the large tensile σ_{xx} mainly results from the effect of concentration gradient. However, σ_{yy} and

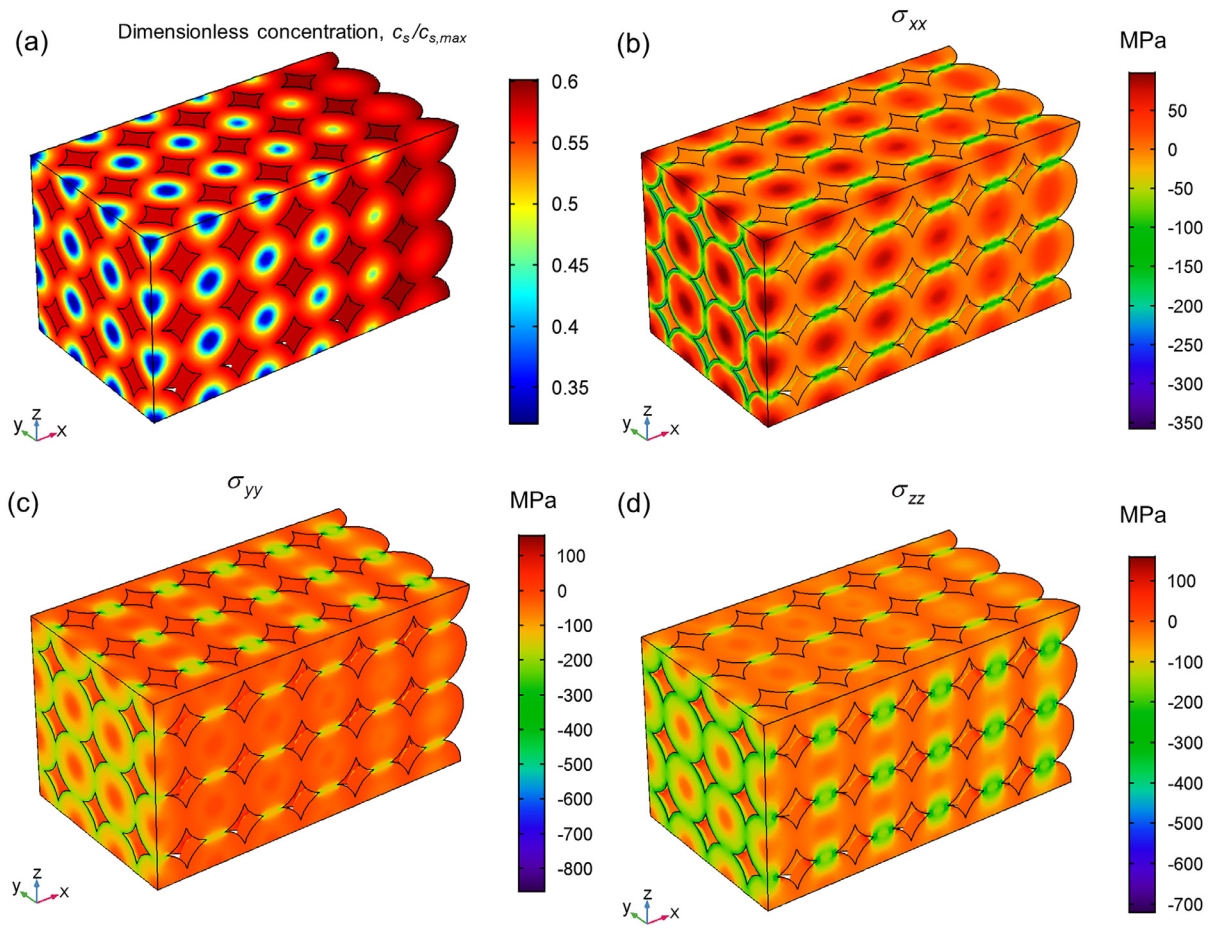

Fig. 7. Distribution of (a) dimensionless concentration, (b) σ_{xx} (c) σ_{yy} and (d) σ_{zz} at the time instant of 500 s.

σ_{zz} at the particle center turn out to be compressive due to the constraints imposed by other particles. Large stresses appear at the particle contact regions due to stress concentration.

5.3. Comparison between two models

The direct three-dimensional particle network model can serve as the benchmark for validation of the multiscale model. This is especially valuable since it is challenging to conduct direct experimental validation against the multiscale model at present: although experimental works focusing on the measurement of deformation or strain of the electrode are available in the literature (Leung et al., 2014; Rieger et al., 2016), the direct measurement of stress distribution inside the particles remains prohibitively difficult. Comparison between the two models demonstrates that the multi-scale model can achieve good satisfying accuracy.

As the first validation, Fig. 8 compares the simulated voltages from the two models. The comparison demonstrates the capability of the multi-scale model to predict the voltage precisely.

Fig. 9 shows the concentration evolution inside a particle at the location of $x/L = 1$. The two models agree well with each other.

In order to compare the stress from the direct three-dimensional particle network model and from the multi-scale model, six points are selected as listed in Table 2. Four points are inside a particle at the location of $x/L = 0.36$. Point A is at the particle center, Points B, C, D are $0.5r_p$ away from Point A along the x, y and z axes, respectively. Points E and F are at r_p away from Point A along the x and z axes, respectively.

The stress from the direct three-dimensional particle network model is shown in solid lines in Fig. 10. To compare these results with the results from the multi-scale model, we first transform the radial and tangential stress (σ_{rr}^c and $\sigma_{\theta\theta}^c$) obtained from the multi-scale model to σ_{xx}^c, σ_{yy}^c and σ_{zz}^c. The coordinate relation is shown in Table 3.

Next, we use the calculated inhomogeneous σ_{ij}^i in the RVE shown in Fig. 6, which has been listed in Table 4, to account for the particle interaction effect. Our purpose is to see whether the stress distribution recovered with RVE can correctly

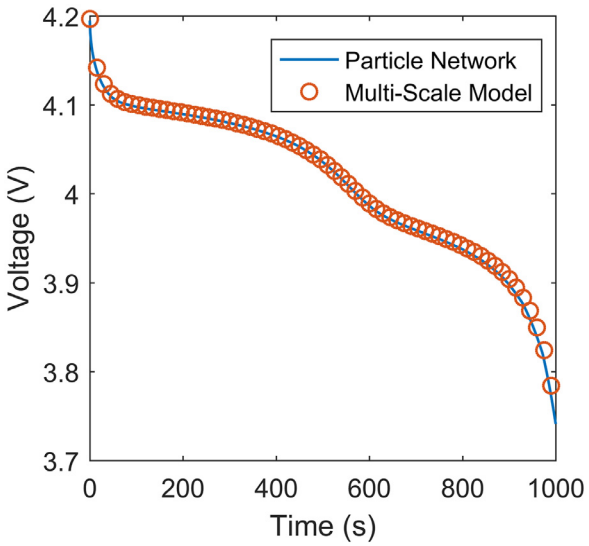

Fig. 8. Comparison of voltages from the direct three-dimensional particle network model (shown in lines) and from the multi-scale model (shown in dots).

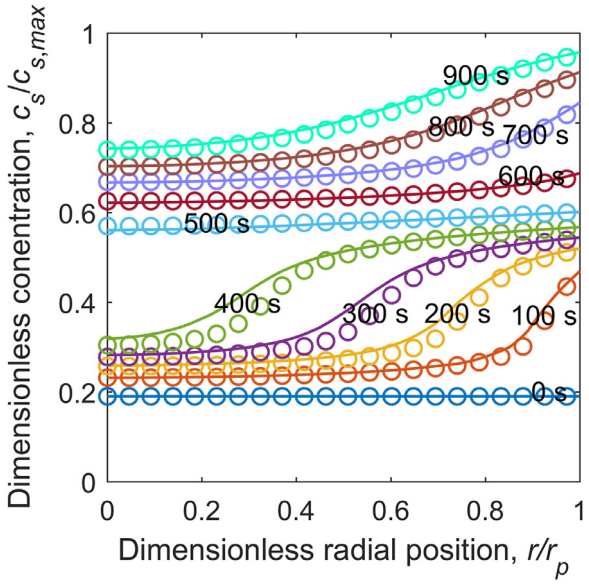

Fig. 9. Comparison of solid dimensionless concentration from the direct three-dimensional particle network model (shown in lines) and from the multi-scale model (shown in dots).

capture the local inhomogeneous stress state. For a given RVE, σ_{ij}^{i} linearly depends on the loads Σ_{yy} and Σ_{zz}. Thus, the temporal profile of σ_{ij}^{i} at any point in the particle can be determined by scaling linearly with the temporal profile of Σ_{yy} and Σ_{zz} as shown in Fig. 5(b).

The total stress based on the multi-scale model is given as $\sigma_{ij}^{c} + \sigma_{ij}^{i}$. Fig. 10 compares the results from the direct three-dimensional particle network model and from the multi-scale model, which shows good agreement at all points.

5.4. Limitations of the multi-scale model

An important assumption of the multi-scale model is the spherically symmetrical concentration distribution at the microscopic particle scale. This assumption is generally justified by the direct three-dimensional particle network simulation results shown in Fig. 7(a). However, a closer investigation shows that this assumption may not be valid in the particle contact regions. As shown in Fig. 11(a), the concentration at the Points E and F differ from that at the solid electrolyte interface. At 300 s, the phase transition induced concentration jump starts to emerge on the particle surface. Without exposure to the

Table 2
Coordinates of points selected for stress comparison.

	Coordinates in direct 3D particle network model	Coordinates in multi-scale model	Coordinates in RVE model
Point A	$x = 0.36L, y = 0.33W, z = 0.66H$	$x = 0.36L, r = 0$	$x = 0, y = 0, z = 0$
Point B	$x = 0.36L + 0.5r_p, y = 0.33W, z = 0.66H$	$x = 0.36L, r = 0.5r_p$	$x = 0.5r_p, y = 0, z = 0$
Point C	$x = 0.36L, y = 0.33W + 0.5r_p, z = 0.66H$	$x = 0.36L, r = 0.5r_p$	$x = 0, y = 0.5r_p, z = 0$
Point D	$x = 0.36L, y = 0.33W, z = 0.66H + 0.5r_p$	$x = 0.36L, r = 0.5r_p$	$x = 0, y = 0, z = 0.5r_p$
Point E	$x = 0.36L + r_p, y = 0.33W, z = 0.66H$	$x = 0.36L, r = r_p$	$x = r_p, y = 0, z = 0$
Point F	$x = 0.36L, y = 0.33W, z = 0.66H + r_p$	$x = 0.36L, r = r_p$	$x = 0, y = 0, z = r_p$

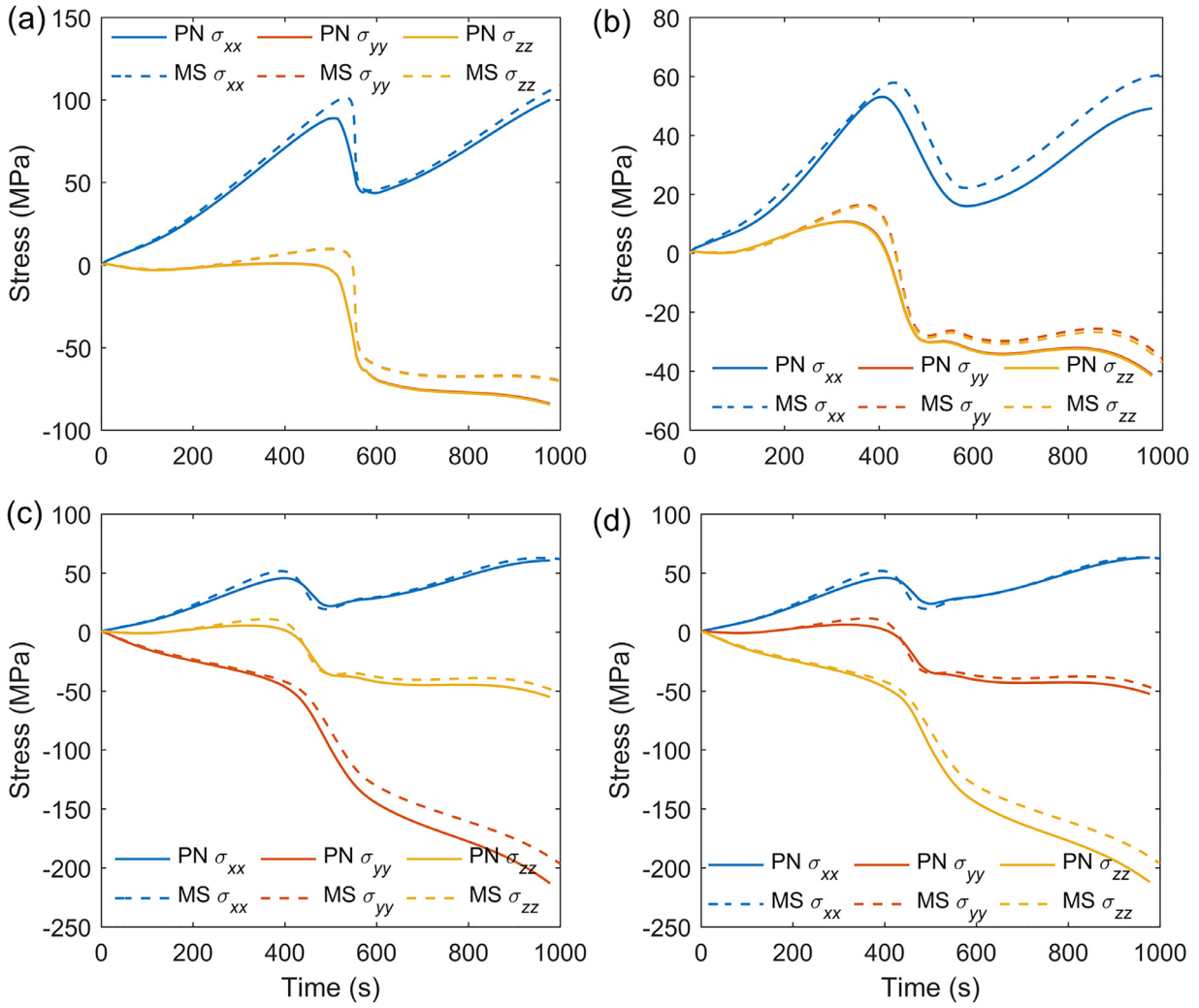

Fig. 10. Comparison of stress from the direct three-dimensional particle network model (shown in solid lines, PN) and from the multi-scale model (shown in dash lines, MS) at (a) Point A, (b) Point B, (c) Point C and (d) Point D.

Table 3
The coordinate relation between σ^c_{xx}, σ^c_{yy}, σ^c_{zz} and σ^c_{rr}, $\sigma^c_{\theta\theta}$ for concentration gradient-induced stress in a particle from the multi-scale model.

	σ^c_{xx}	σ^c_{yy}	σ^c_{zz}
Point A	$\sigma^c_{rr}(r = 0)$	$\sigma^c_{rr}(r = 0)$	$\sigma^c_{rr}(r = 0)$
Point B	$\sigma^c_{rr}(r = 0.5r_p)$	$\sigma^c_{\theta\theta}(r = 0.5r_p)$	$\sigma^c_{\theta\theta}(r = 0.5r_p)$
Point C	$\sigma^c_{\theta\theta}(r = 0.5r_p)$	$\sigma^c_{rr}(r = 0.5r_p)$	$\sigma^c_{\theta\theta}(r = 0.5r_p)$
Point D	$\sigma^c_{\theta\theta}(r = 0.5r_p)$	$\sigma^c_{\theta\theta}(r = 0.5r_p)$	$\sigma^c_{rr}(r = 0.5r_p)$
Point E	$\sigma^c_{rr}(r = r_p) = 0$	$\sigma^c_{\theta\theta}(r = r_p)$	$\sigma^c_{\theta\theta}(r = r_p)$
Point F	$\sigma^c_{\theta\theta}(r = r_p)$	$\sigma^c_{\theta\theta}(r = r_p)$	$\sigma^c_{rr}(r = r_p) = 0$

Table 4
Interaction stress in the RVE under the boundary loads of $\Sigma_{xx} = 0$, $\Sigma_{yy} = \Sigma_{zz} = -27$ MPa.

	σ^i_{xx}	σ^i_{yy}	σ^i_{zz}
Point A	31.9 MPa	−55.2 MPa	−55.4 MPa
Point B	14.1 MPa	−26.3 MPa	−27.0 MPa
Point C	21.3 MPa	−111.2 MPa	−34.2 MPa
Point D	21.5 MPa	−33.4 MPa	−111.1 MPa
Point E	1.8 MPa	3.3 MPa	3.4 MPa
Point F	−73.9 MPa	−102.6 MPa	−143.1 MPa

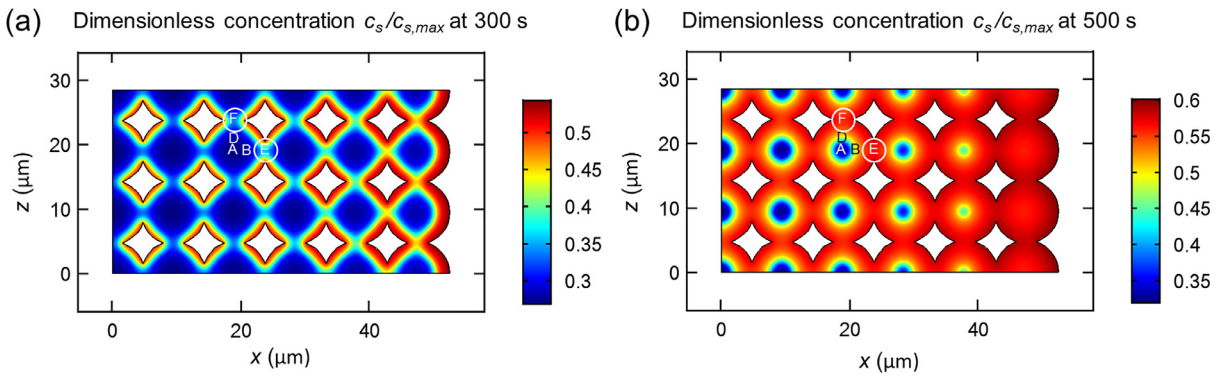

Fig. 11. Distribution of lithium concentration in particles at (a) 300 s and (b) 500 s from the direct three-dimensional particle network simulation. The two-dimensional slice is at $y = 0.33$ W in Fig. 2.

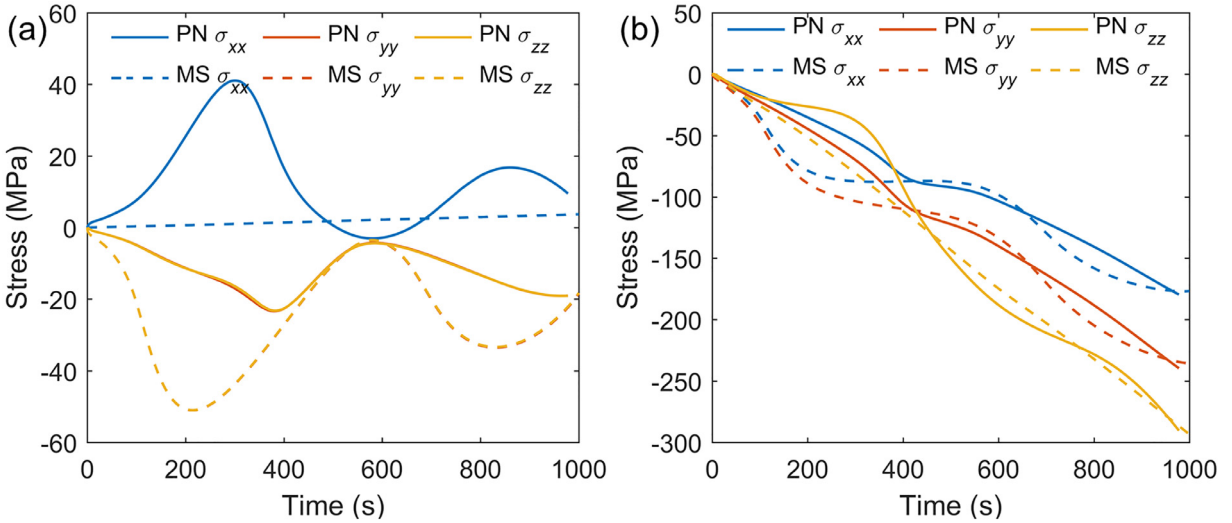

Fig. 12. Comparison of stress from the direct three-dimensional particle network model (shown in solid lines, PN) and from the multi-scale model (shown in dash lines, MS) at (a) Point E and (b) Point F.

electrolyte, the particle overlapping region does now allow direct intercalation of lithium ions from the electrolyte at Points E and F: it has to wait for the relatively slow solid diffusion to become lithiated. However, the solid diffusion is associated with a rather sharp concentration jump, thus Points E and F exhibit significantly different concentration than other particle surface points. When the concentration jump moves inside the particles at 500 s, the electrode shows a spherically symmetrical distribution of concentration surrounding each particle as in Fig. 11(b). This mechanism cannot be captured by the multi-scale model which does not consider detailed particle structure: all surface points of particles, including Points E and F, are considered to be directly exposed to the electrolyte.

The asymmetrical concentration distribution shown in Fig. 11(a) leads to a difference of stress predicted with the two models, as shown in Fig. 12. To understand the mechanical effect of large local concentration gradient at Points E and F, we can treat these two points as if they are at the centers of two small virtual “particles” noted by the white circles in Fig. 11.

At 300 s, Points E and F undergo tensile stress because the outer parts of "particles" have much larger lithium concentration. This explains why the solid lines are higher than their dash line counterparts at 300 s in Fig. 12. In addition, the gap between two corresponding lines for each stress component is similar at 300 s, because the stress due to local concentration gradient at the "particle" center is almost hydrostatic. The two models agree well with each other at 500 s, as shown in Fig. 11(b), because by now the inhomogeneous concentration distribution on a particle surface between the particle contact regions and no contact regions has vanished.

We also note that the two models agree better at Point F than at Point E. As there is no constraint for the electrode expansion along the x direction, the particle interaction stress σ_{ij}^{i} is much smaller at Point E than at Point F, which can be seen in Table 4. Thus, the stress at Point E depends more on the concentration in the particle. The multiscale model captures the intra-particle concentration gradient-induced stress σ_{ij}^{c} but does not address any asymmetrical inter-particle concentration distribution. In contrast, the stress at Point F can be predicted well using our multiscale model except for the period when phase transition induces sharp inter-particle concentration gradient.

6. Conclusions

We have developed two models, a multi-scale model and a direct three-dimensional particle network model, to fully couple mechanics and electrochemistry consistently at both micro and continuum scales.

The pseudo-2D model based on porous electrode theory is widely used in the field of electrochemistry due to its efficiency and predicting capability without the need to directly model detailed particle configurations. The multi-scale model developed in this work offers similar advantage. The electrochemical part of the multiscale model is consistent with the pseudo-2D model with several important revisions. First, we extend the solid diffusion equation using the OCP curve and its derived thermodynamic factor to account for the phase transition effect. This revision is important since the phase transition can lead to large concentration gradient inside the particle, which further results in large concentration gradient induced-stress. Second, we include the effect of stress on the electrochemical reaction kinetics in addition to the stress effect on solid diffusion, which fully couples electrochemical and mechanical behaviors. The mechanical stress in the particle is described by the superposition of concentration gradient-induced stress and particle interaction stress. The concentration gradient-induced stress is given by the solid concentration profile while the particle interaction stress is captured by the continuum scale stress. The detailed information such as local contact stress concentration can be recovered by performing a RVE calculation of a representative particle structure with the continuum scale stress at the boundary loads.

In this paper we considered uniform particle size as an example to demonstrate the multiscale model. One can readily consider a distribution of particle sizes along the electrode thickness by taking $r_p = r_p(x)$ instead of a constant r_p, or extend to three dimensional distribution. One can also address locally mixed particle sizes, e.g. using a mixture of two sizes of particles for the electrode, by considering two representative particles. The equations for each particle are the same as shown in this paper, except that the homogenization should be taken over the two particles to connect particle scale quantities such as stress and intercalation current density to the continuum scale equations. We expect that such a mixed particle system will demonstrate rich behaviors. For instance, smaller particles may intercalate and swell faster than larger particles in the same region. This will change the stress state of surrounding neighbors in a manner different than uniform simultaneous swelling of particles with the same size. In this paper we considered particles to be spherical, which is a reasonable representation of the shape of many active material particles. It is possible to engineer particles into other geometries such as disc or rod shapes. In such cases, one can consider ellipsoidal particles and use the orientation distribution function to describe their orientations. A distinct effect is that if the orientation distribution is not random, the active material will exhibit anisotropic reaction rates and interactions in the electrode.

The three-dimensional particle network model directly models the particle network explicitly using fully coupled electrochemical-mechanical equations. This model can be applied to arbitrary particle geometries and networks, but is associated with high computational cost. Using the three-dimensional particle network model as a benchmark, we validate the accuracy of the multi-scale model. The comparison shows that the two models agree well in both the electrochemical behaviors and the local stress distribution, which demonstrates the capability of the multiscale model in predicting coupled electrochemical-mechanical behaviors. Deviation from the three-dimensional particle network model occurs only when the concentration in the particle is highly different from spherical symmetry. In other words, the multiscale model can be applied to all situations where the standard pseudo-2D electrochemical model is applicable.

We envision that the multi-scale model can be used to address various coupled mechanical-electrochemical problems at continuum scale such as cracking in-between particles, delamination of the electrode from the current collector, and evaluation of the impact of fracture and other defects on battery performance. The three-dimensional particle network model allows studying coupled processes related to particle network details, such as particle shape and size distribution on battery performance, intra-particle fracture in inhomogeneous environment, and deboning of individual particles from the network.

Acknowledgment

This work was supported by the National Science Foundation under Grant No. CNS-1446117.

Appendix A. Solid diffusion with mechanical stress

In this work, we follow the modeling framework of (Baker et al., 2016) to consider the coupled stress and diffusion in solids. The solid is assumed to consist of a lattice network, which undergoes mechanical deformation and stress. Three species (lithium, host material and vacancy) occupy the lattice sites, and their total number is conserved. The host material, i.e. Mn_2O_4 in this work, is considered immobile, while the lithium and vacancy can exchange lattice sites with each other. The lithium diffusion process is in nature a process that lithium gradually occupies the vacancy sites, i.e. $\mathbf{N}_{\mathrm{Li}-\Theta} + \mathbf{N}_{\Theta} = \mathbf{0}$, where $\mathbf{N}_{\mathrm{Li}-\Theta}$ is the lithium flux and $\mathbf{N}_{\Theta}$ is the vacancy flux. Here we use the subscript 'Θ' to denote vacancy and the substrate '$\mathrm{Li}-\Theta$' to denote lithium ion while highlighting the existence of vacancy.

As the lithiation-induced volume change in $LiMn_2O_4$ is small, we consider the deformation as infinitesimal. Thus, the solid lithium concentration described using the Lagrangian coordinate system is the same as that using the Euler coordinate system. The convective lithium flux in solid due to lattice expansion is also assumed as zero (see Eq. (18) in (Baker et al., 2016)).

The lithium diffusional flux is governed by the gradient of chemical potential,

$$\mathbf{N}_{\mathrm{Li}-\Theta} = -\mathbf{N}_{\Theta} = -L\nabla(\mu_{\mathrm{Li}-\Theta} - \mu_{\Theta}), \tag{A1}$$

where the coefficient L can be determined using the Stefan–Maxwell equation. After some algebraic manipulations, the flux is given by (Baker et al., 2016)

$$\mathbf{N}_{\mathrm{Li}-\Theta} = -\frac{D_0}{RT}c_{s,max}\left(\frac{c_s}{c_{s,max}}\right)\left(1-\frac{c_s}{c_{s,max}}\right)\nabla(\mu_{\mathrm{Li}-\Theta} - \mu_{\Theta}). \tag{A2}$$

The chemical potential is given by

$$\begin{aligned}\mu_{\mathrm{Li}-\Theta} &= \mu^0_{\mathrm{Li}-\Theta} + RT\ln a_{\mathrm{Li}-\Theta} - \Omega_{\mathrm{Li}-\Theta}\sigma_h,\\ \mu_{\Theta} &= \mu^0_{\Theta} + RT\ln a_{\Theta} - \Omega_{\Theta}\sigma_h,\end{aligned} \tag{A3}$$

where μ^0_i represents the standard state chemical potential of phase i, a_i is the activity of phase i, Ω_i is the partial molar volume of phase i and σ_h is the hydrostatic stress experienced by the lattice network. The chemical potential of lithium in active particles used in Eq. (11), μ, is rigorously defined as

$$\mu = \mu_{\mathrm{Li}-\Theta} - \mu_{\Theta}. \tag{A4}$$

Thus,

$$\nabla\mu = \nabla(\mu_{\mathrm{Li}-\Theta} - \mu_{\Theta}) = RT\nabla(\ln a_{\mathrm{Li}-\Theta} - \ln a_{\Theta}) - \Omega\nabla\sigma_h, \tag{A5}$$

where $\Omega = \Omega_{\mathrm{Li}-\Theta} - \Omega_{\Theta}$ is the partial molar volume of lithium in the solid.

The activity can be related to the measured open circuit potential, E_{ref}. E_{ref} is usually measured as the open circuit potential of a $LiMn_2O_4$-Li half-cell under equilibrium conditions, where the solid lithium concentration and electrolyte lithium concentration are both uniform, and there is no mechanical stress. The overall reaction of the half-cell is

$$\mathrm{Li}-\Theta \leftrightharpoons \mathrm{Li} + \Theta. \tag{A6}$$

Thus, E_{ref} can be obtained by the Nernst equation as

$$E_{ref} = E^0_{ref} + \frac{RT}{F}\ln\left(\frac{a_{\Theta}}{a_{\mathrm{Li}-\Theta}}\right), \tag{A7}$$

where $E^0_{ref} = (\mu^0_{\mathrm{Li}} + \mu^0_{\Theta} - \mu^0_{\mathrm{Li}-\Theta})/F$ and μ^0_{Li} is the chemical potential of pure lithium metal. E^0_{ref} is constant because μ^0_{Li}, μ^0_{Θ} and $\mu^0_{\mathrm{Li}-\Theta}$ are all constant. Thus,

$$RT\nabla(\ln a_{\mathrm{Li}-\Theta} - \ln a_{\Theta}) = -F\nabla E_{ref} = \frac{-FK}{c_{s,max}}\nabla c_s, \tag{A8}$$

where $K = \partial E_{ref}/\partial x_{Li}$. Combining Eqs. (A2) (A5) and (A8), we have

$$\mathbf{N}_{\mathrm{Li}-\Theta} = \frac{D_0}{RT}\left(\frac{c_s}{c_{s,max}}\right)\left(1-\frac{c_s}{c_{s,max}}\right)(FK\nabla c_s + \Omega c_{s,max}\nabla\sigma_h). \tag{A9}$$

This equation is the same as Eq. (17) or Eq. (39), where $\mathbf{N}_s$ is $\mathbf{N}_{\mathrm{Li}-\Theta}$.

Appendix B. Charge transfer kinetics with mechanical stress

The lithium intercalation or deintercalation reaction can be written as

$$\mathrm{Li}-\Theta \leftrightharpoons \mathrm{Li}^+ + \mathrm{e}^- + \Theta \tag{B1}$$

where Li^+ represents the lithium ion in the electrolyte, e^- represents the electron, Θ represents the intercalation site in the electrode solid, and Li-Θ represents the lithium in the electrode solid.

The forward and backward reaction rates, $r_\rightarrow$ and $r_\leftarrow$, are given by the transition state theory,

$$r_\rightarrow = r_0 \exp\left(-\frac{\mu_{TS} - \mu_{\mathrm{Li}-\Theta}}{RT}\right),$$
$$r_\leftarrow = r_0 \exp\left(-\frac{\mu_{TS} - (\mu_{\mathrm{Li}^+} + \mu_{\mathrm{e}^-} + \mu_\Theta)}{RT}\right). \tag{B2}$$

Here r_0 is a rate constant, μ_i represents the chemical potential of phase i and 'TS' stands for the transition state. The expressions of the reactant chemical potentials can be written as

$$\begin{aligned}
\mu_{\mathrm{Li}-\Theta} &= \mu^0_{\mathrm{Li}-\Theta} + RT \ln a_{\mathrm{Li}-\Theta},\\
\mu_\Theta &= \mu^0_\Theta + RT \ln a_\Theta,\\
\mu_{\mathrm{Li}^+} &= \mu^0_{\mathrm{Li}^+} + RT \ln a_{\mathrm{Li}^+} + F\phi_e,\\
\mu_{\mathrm{e}^-} &= -F\phi_s,
\end{aligned} \tag{B3}$$

where a_i is the activity of phase i, ϕ_e is the electric potential of electrolyte near the interface, and ϕ_s is the electric potential of solid near the interface. Note that ϕ_e and ϕ_s should be defined with respect to the same reference point, say the current collector of the negative electrode. If so, ϕ_s is equivalent to Φ_s used in Eq. (22) while ϕ_e is different from Φ_e but their relation will be given later. The transition state chemical potential is given by

$$\mu_{TS} = \mu^0_{TS} + (1-\beta)F(\phi_e - \phi_s), \tag{B4}$$

where β is the cathodic symmetry factor, which represents the fraction of applied potential in promoting the cathodic reaction, i.e. the backward reaction in Eq. (B2).

With Eqs. (B3) and (B4), the forward and backward reaction rates are given by

$$r_\rightarrow = r_0 \exp\left(-\frac{\mu^0_{TS} - \mu^0_{\mathrm{Li}-\Theta}}{RT}\right) a_{\mathrm{Li}-\Theta} \exp\left(-\frac{(1-\beta)F(\phi_e - \phi_s)}{RT}\right),$$
$$r_\leftarrow = r_0 \exp\left(-\frac{\mu^0_{TS} - \mu^0_\Theta - \mu^0_{\mathrm{Li}^+}}{RT}\right) a_{\mathrm{Li}^+} a_\Theta \exp\left(\frac{\beta F(\phi_e - \phi_s)}{RT}\right). \tag{B5}$$

The anodic and cathodic reaction rate constants are defined as

$$k_a = r_0 \exp\left(-\frac{\mu^0_{TS} - \mu^0_{\mathrm{Li}-\Theta}}{RT}\right), k_c = r_0 \exp\left(-\frac{\mu^0_{TS} - \mu^0_\Theta - \mu^0_{\mathrm{Li}^+}}{RT}\right). \tag{B6}$$

Then, the net reaction rate is

$$\begin{aligned}
r &= r_\rightarrow - r_\leftarrow\\
&= k_a a_{\mathrm{Li}-\Theta} \exp\left(\frac{(1-\beta)F(\phi_s - \phi_e)}{RT}\right) - k_c a_{\mathrm{Li}^+} a_\Theta \exp\left(-\frac{\beta F(\phi_s - \phi_e)}{RT}\right).
\end{aligned} \tag{B7}$$

A typical method to simplify Eq. (B7) is to introduce the equilibrium potential,

$$(\phi_s - \phi_e)_{\mathrm{eq}} = U = \frac{RT}{F} \ln\left(\frac{k_c}{k_a}\right) + \frac{RT}{F} \ln\left(\frac{a_{\mathrm{Li}^+} a_\Theta}{a_{\mathrm{Li}-\Theta}}\right), \tag{B8}$$

which results in zero net reaction rate. This gives

$$U = \frac{\mu_\Theta + \mu^0_{\mathrm{Li}^+} + RT \ln a_{\mathrm{Li}^+} - \mu_{\mathrm{Li}-\Theta}}{F}. \tag{B9}$$

Note that Udepends on both the electrolyte lithium concentration and the solid lithium concentration, which differs from the E_{ref} in Eq. (22), which only depends on the solid lithium concentration.

The overpotential is defined as

$$\eta = \phi_s - \phi_e - U. \tag{B10}$$

Then, the charge transfer current can be given as

$$i = rF = i_0 \left[\exp\left(\frac{(1-\beta)F\eta}{RT}\right) - \exp\left(-\frac{\beta F\eta}{RT}\right)\right], \tag{B11}$$

where the exchange current density is given by

$$i_0 = F(k_a a_{\mathrm{Li}-\Theta})^\beta (k_c a_{\mathrm{Li}^+} a_\Theta)^{1-\beta}. \tag{B12}$$

Next, we should establish a relation between ϕ_e and Φ_e, and another relation between U and E_{ref}. At the point of interest that has a "real" electrolyte potential of ϕ_e, we put a lithium metal reference electrode, and measure the potential difference between this reference electrode with respect to the chosen fixed point. The measurement potential under equilibrium is Φ_e. The reaction at this reference electrode is given as

$$\mathrm{Li} \leftrightharpoons \mathrm{Li}^+ + \mathrm{e}^-. \tag{B13}$$

The equilibrium condition of reaction gives

$$\mu^0_{\mathrm{Li}} = \mu^0_{\mathrm{Li}^+} + RT \ln a_{\mathrm{Li}^+} + F\phi_e - F\Phi_e, \tag{B14}$$

where μ^0_{Li} is the chemical potential of pure lithium metal. Thus,

$$\Phi_e = \phi_e + \frac{\mu^0_{\mathrm{Li}^+} + RT \ln a_{\mathrm{Li}^+} - \mu^0_{\mathrm{Li}}}{F}. \tag{B15}$$

E_{ref} is usually measured as the open circuit potential of a half-cell under equilibrium conditions with lithium metal as the negative electrode, where the solid lithium concentration and electrolyte lithium concentration are both uniform. The overall reaction of the half-cell is

$$\mathrm{Li} - \Theta \leftrightharpoons \mathrm{Li} + \Theta. \tag{B16}$$

Thus, E_{ref} can be given by the Nernst equation as

$$E_{ref} = \frac{\mu^0_{\mathrm{Li}} + \mu_\Theta - \mu_{\mathrm{Li}-\Theta}}{F}. \tag{B17}$$

Note that no electrolyte lithium concentration appears in Eq. (B17). Combining Eqs. (B9), (B15) and (B17), the overpotential in Eq. (B10) can be re-written as

$$\eta = \Phi_s - \Phi_e - E_{ref}, \tag{B18}$$

which is what we used in this paper.

Now, we consider the influence of mechanical stress on the charge transfer kinetics. The mechanical stress has no effect on the chemical potential of electrolyte lithium ions and electrons, but adds additional terms in $\mu_{\mathrm{Li}-\Theta}$ and μ_Θ,

$$\begin{aligned} \mu_{\mathrm{Li}-\Theta} &= \mu^0_{\mathrm{Li}-\Theta} + RT \ln a_{\mathrm{Li}-\Theta} - \Omega_{\mathrm{Li}-\Theta}\sigma_h, \\ \mu_\Theta &= \mu^0_\Theta + RT \ln a_\Theta - \Omega_\Theta \sigma_h, \end{aligned} \tag{B19}$$

where Ω_i is the partial molar volume of phase i and σ_h is the hydrostatic stress.

The transition state energy is given by

$$\mu_{TS} = \mu^0_{TS} + (1-\beta)F(\phi_e - \phi_s) + \beta_m(-\Omega_{\mathrm{Li}-\Theta}\sigma_h) + (1-\beta_m)(-\Omega_\Theta\sigma_h), \tag{B20}$$

where β_m is the mechanically cathodic symmetry factor. The forward and backward reaction rates are then given by

$$\begin{aligned} r_\rightarrow &= r_0 \exp\left(-\frac{\mu^0_{TS} - \mu^0_{\mathrm{Li}-\Theta}}{RT}\right) a_{\mathrm{Li}-\Theta} \exp\left(-\frac{(1-\beta)F(\phi_e - \phi_s)}{RT}\right) \exp\left(-\frac{(1-\beta_m)\Omega\sigma_h}{RT}\right), \\ r_\leftarrow &= r_0 \exp\left(-\frac{\mu^0_{TS} - \mu^0_\Theta - \mu^0_{\mathrm{Li}^+}}{RT}\right) a_{\mathrm{Li}^+} a_\Theta \exp\left(\frac{\beta F(\phi_e - \phi_s)}{RT}\right) \exp\left(\frac{\beta_m \Omega\sigma_h}{RT}\right), \end{aligned} \tag{B21}$$

where $\Omega = \Omega_{\mathrm{Li}-\Theta} - \Omega_\Theta$ is the partial molar volume of lithium in the solid.

Thus, the net reaction rate is

$$\begin{aligned} r &= r_\rightarrow - r_\leftarrow \\ &= k_a a_{\mathrm{Li}-\Theta} \exp\left(\frac{(1-\beta)F(\phi_s - \phi_e)}{RT} - \frac{(1-\beta_m)\Omega\sigma_h}{RT}\right) - k_c a_{\mathrm{Li}^+} a_\Theta \exp\left(-\frac{\beta F(\phi_s - \phi_e)}{RT} + \frac{\beta_m \Omega\sigma_h}{RT}\right), \end{aligned} \tag{B22}$$

Similarly, we introduce the equilibrium potential with the influence of mechanical stress as

$$(\phi_s - \phi_e)_{\mathrm{eq}} = U_m = \frac{RT}{F}\ln\left(\frac{k_c}{k_a}\right) + \frac{RT}{F}\ln\left(\frac{a_{\mathrm{Li}^+} a_\Theta}{a_{\mathrm{Li}-\Theta}}\right) + \frac{\Omega\sigma_h}{F}, \tag{B23}$$

and the revised overpotential as

$$\eta_m = \phi_s - \phi_e - U_m, \tag{B24}$$

then the charge transfer current is given by

$$i = rF = i_0 \exp\left[\frac{(\beta_m - \beta)\Omega\sigma_h}{RT}\right]\left[\exp\left(\frac{(1-\beta)F\eta_m}{RT}\right) - \exp\left(-\frac{\beta F\eta_m}{RT}\right)\right]. \tag{B25}$$

Following the same procedure to remove the dependence of equilibrium potential on electrolyte lithium concentration, we can get

$$\eta_m = \Phi_s - \Phi_e - E_{ref} - \frac{\Omega\sigma_h}{F}. \tag{B26}$$

Note that the exchange current density given by Eq. (B12) depends on activity instead of concentration. Rigorously speaking, the activity of solid phase can be derived and fitted from the measured E_{ref} (see more in (Colclasure and Kee, 2010; Karthikeyan et al., 2008; Latz and Zausch, 2013; Zhang et al., 2006)). In this work, we utilize the common approximation in the porous electrode model to replace the activity with concentration, which gives

$$i_0 = F(k_a c_{\mathrm{Li-}\Theta})^{\beta}(k_c c_{\mathrm{Li^+}} c_{\Theta})^{1-\beta} = Fkc_{s,surf}^{\beta} c_e^{1-\beta}(c_{s,max} - c_{s,surf})^{1-\beta} \tag{B27}$$

Appendix C. Determination of elastic modulus and expansion coefficient using asymptotic homogenization method

As derived in (Pinho-da-Cruz et al., 2009), the homogenized elastic tensor using the asymptotic homogenization method is

$$C_{ijmn}^H = \frac{1}{|Y|}\int_Y C_{ijkl}(\mathbf{y})\left(I_{kl}^{mn} - \frac{\partial \chi_k^{mn}}{\partial y_l}\right)dY, \tag{C1}$$

where Ydenotes a periodic RVE structure whose volume is denoted as $|Y|$, $\mathbf{y}$ is the coordinate system in the RVE (note that here we use y_1, y_2, y_3 instead of x, y, z to denote the components of the RVE coordinate system), $C_{ijkl}(\mathbf{y})$is either the elastic modulus of particles or zero depending on the location $\mathbf{y}$, $I_{kl}^{mn} = \delta_{mk}\delta_{nl}$ with δ_{ij} being Kronecker delta, χ_k^{mn} is the characteristic displacement field tensor, and $dY = dy_1 dy_2 dy_3$. The asymptotic homogenization method has developed an approach to calculate χ_k^{mn}, and then the homogenized elastic modulus using Eq. (C1).

χ_k^{mn} is a third-order tensor with the symmetry of $\chi_k^{mn} = \chi_k^{nm}$, and is given by

$$\frac{\partial}{\partial y_j}\left[C_{ijkl}(\mathbf{y})\left(I_{kl}^{mn} - \frac{\partial \chi_k^{mn}}{\partial y_l}\right)\right] = 0. \tag{C2}$$

The periodic structure gives the following periodic boundary conditions

$$\begin{aligned}
\chi_k^{mn}(0, y_2, y_3) &= \chi_k^{mn}(y_1^0, y_2, y_3),\\
\chi_k^{mn}(y_1, 0, y_3) &= \chi_k^{mn}(y_1, y_2^0, y_3),\\
\chi_k^{mn}(y_1, y_2, 0) &= \chi_k^{mn}(y_1, y_2, y_3^0),
\end{aligned} \tag{C3}$$

where y_1^0, y_2^0, y_3^0 are the length of RVE along the y_1, y_2, y_3 axes and $y_1 \in [0, y_1^0]$, $y_2 \in [0, y_2^0]$, and $y_3 \in [0, y_3^0]$. We also need to impose a fixed constraint at one point to eliminate the singularity, which can be given as

$$\chi_k^{mn}(0, 0, 0) = 0. \tag{C4}$$

The calculated results for the continuum scale mechanical properties are

$$\begin{aligned}
&C_{1111}^H = C_{2222}^H = C_{3333}^H = 2.43\ \mathrm{GPa},\\
&C_{1122}^H = C_{2211}^H = C_{1133}^H = C_{3311}^H = C_{2233}^H = C_{3322}^H = 0.374\ \mathrm{GPa},\\
&C_{1212}^H = C_{2323}^H = C_{1313}^H = 0.80\ \mathrm{GPa},
\end{aligned} \tag{C5}$$

and other elastic components are zero. Using the matrix expression, the elastic modulus can be written as

$$\mathbf{C}^H = \begin{bmatrix} 2.43 & 0.374 & 0.374 & & & \\ 0.374 & 2.43 & 0.374 & & & \\ 0.374 & 0.374 & 2.43 & & & \\ & & & 0.80 & & \\ & & & & 0.80 & \\ & & & & & 0.80 \end{bmatrix}\mathrm{GPa}. \tag{C6}$$

The calculated results show that the homogenized elastic modulus has only three independent components, $E^H = 2.33$ GPa, $\nu^H = 0.13$, $G^H = 0.80$ GPa. See more at (Penta and Gerisch, 2015).

If we treat the concentration in analogy as temperature, the determination of homogenized $\Omega^H$is equivalent to the determination of homogenized thermal expansion coefficient α_{ij}^H. As given in (Shabana and Noda, 2008), α_{ij}^H is given by

$$\alpha_{ij}^H = S_{ijpq}^H \frac{1}{|Y|}\int_Y C_{pqkl}(\mathbf{y})\left(\alpha_{kl}(\mathbf{y}) - \frac{\partial \varphi_k}{\partial y_l}\right)dY, \tag{C7}$$

where S^H_{ijkl} is the homogenized compliance tensor, which is the inverse of C^H_{ijkl}. The thermal expansion coefficient of the particle is isotropic as $\alpha_{11} = \alpha_{22} = \alpha_{33} = \Omega, \alpha_{ij} = 0 (i \neq j)$, and the thermal expansion of the pore is always 0. The characteristic displacement φ_k in Eq. (C7) is determined by

$$\frac{\partial}{\partial y_j}\left[C_{ijkl}(\mathbf{y})\left(\alpha_{kl}(\mathbf{y}) - \frac{\partial \varphi_k}{\partial y_l}\right)\right] = 0. \tag{C8}$$

The calculated result is $\alpha^H_{ij} = \alpha_{ij}$. Thus, $\Omega^H = \Omega$.

References

Baker, D.R., Verbrugge, M.W., Bower, A.F., 2016. Thermodynamics, stress, and Stefan–Maxwell diffusion in solids: application to small-strain materials used in commercial lithium-ion batteries. J. Solid State Electrochem. 20, 163–181.

Benveniste, Y., 1987. A new approach to the application of Mori-Tanaka's theory in composite materials. Mech. Mater. 6, 147–157.

Bhandakkar, T.K., Gao, H.J., 2010. Cohesive modeling of crack nucleation under diffusion induced stresses in a thin strip: implications on the critical size for flaw tolerant battery electrodes. Int. J. Solids Struct. 47, 1424–1434.

Bhandakkar, T.K., Gao, H.J., 2011. Cohesive modeling of crack nucleation in a cylindrical electrode under axisymmetric diffusion induced stresses. Int. J. Solids Struct. 48, 2304–2309.

Bohn, E., Eckl, T., Kamlah, M., McMeeking, R., 2013. A model for lithium diffusion and stress generation in an intercalation storage particle with phase change. J. Electrochem. Soc. 160, A1638–A1652.

Christensen, J., Newman, J., 2006. Stress generation and fracture in lithium insertion materials. J. Solid State Electrochem. 10, 293–319.

Colclasure, A.M., Kee, R.J., 2010. Thermodynamically consistent modeling of elementary electrochemistry in lithium-ion batteries. Electrochim. Acta 55, 8960–8973.

Dai, Y., Cai, L., White, R.E., 2014. Simulation and analysis of stress in a Li-ion battery with a blended LiMn2O4 and LiNi0.8Co0.15Al0.05O2 cathode. J. Power Sources 247, 365–376.

Deshpande, R., Cheng, Y.T., Verbrugge, M.W., 2010. Modeling diffusion-induced stress in nanowire electrode structures. J. Power Sources 195, 5081–5088.

Doyle, M., Fuller, T.F., Newman, J., 1993. Modeling of galvanostatic charge and discharge of the lithium polymer insertion cell. J. Electrochem. Soc. 140, 1526–1533.

Hill, R., 1965. A self-consistent mechanics of composite materials. J. Mech. Phys. Solids 13, 213–222.

Jia, Z., Liu, W.K., 2016. Analytical model on stress-regulated lithiation kinetics and fracture of Si-C yolk-shell anodes for lithium-ion batteries. J Electrochem. Soc. 163, A940–A946.

Karthikeyan, D.K., Sikha, G., White, R.E., 2008. Thermodynamic model development for lithium intercalation electrodes. J. Power Sources 185, 1398–1407.

Kim, S., Choi, S.J., Zhao, K., Yang, H., Gobbi, G., Zhang, S., Li, J., 2016. Electrochemically driven mechanical energy harvesting. Nat. Commun. 7, 10146.

Latz, A., Zausch, J., 2013. Thermodynamic derivation of a Butler-Volmer model for intercalation in Li-ion batteries. Electrochim. Acta 110, 358–362.

Leung, P.K., Moreno, C., Masters, I., Hazra, S., Conde, B., Mohamed, M.R., Dashwood, R.J., Bhagat, R., 2014. Real-time displacement and strain mappings of lithium-ion batteries using three-dimensional digital image correlation. J. Power Sources 271, 82–86.

Liu, H., Wolf, M., Karki, K., Yu, Y.-S., Stach, E.A., Cabana, J., Chapman, K.W., Chupas, P.J., 2017. Intergranular cracking as a major cause of long-term capacity fading of layered cathodes. Nano Lett. 17, 3452–3457.

Mendoza, H., Roberts, S.A., Brunini, V.E., Grillet, A.M., 2016. Mechanical and electrochemical response of a $LiCoO_2$ cathode using reconstructed microstructures. Electrochim. Acta 190, 1–15.

Monroe, C., Newman, J., 2005. The impact of elastic deformation on deposition kinetics at lithium/polymer interfaces. J. Electrochem. Soc. 152, A396–A404.

Mori, T., Tanaka, K., 1973. Average stress in matrix and average elastic energy of materials with misfitting inclusions. Acta Metallurg. 21, 571–574.

Newman, J.S., 1991. Electrochemical Systems, Second ed. Prentice Hall, Englewood Cliffs, N.J.

Penta, R., Gerisch, A., 2015. Investigation of the potential of asymptotic homogenization for elastic composites via a three-dimensional computational study. Comput. Vis. Sci. 17, 185–201.

Pinho-da-Cruz, J., Oliveira, J.A., Teixeira-Dias, F., 2009. Asymptotic homogenisation in linear elasticity. Part I : mathematical formulation and finite element modelling. Comput. Mater. Sci. 45, 1073–1080.

Purkayastha, R., McMeeking, R., 2013. A parameter study of intercalation of lithium into storage particles in a lithium-ion battery. Comput. Mater. Sci. 80, 2–14.

Purkayastha, R.T., McMeeking, R.M., 2012. An integrated 2-D model of a lithium ion battery: the effect of material parameters and morphology on storage particle stress. Comput. Mech. 50, 209–227.

Rieger, B., Schlueter, S., Erhard, S.V., Jossena, A., 2016. Strain propagation in lithium-ion batteries from the crystal structure to the electrode level. J. Electrochem. Soc. 163, A1595–A1606.

Roberts, A.P., Garboczi, E.J., 2000. Elastic properties of model porous ceramics. J. Am. Ceram. Soc. 83, 3041–3048.

Roberts, S.A., Brunini, V.E., Long, K.N., Grillet, A.M., 2014. A framework for three-dimensional mesoscale modeling of anisotropic swelling and mechanical deformation in lithium-ion electrodes. J. Electrochem. Soc. 161, F3052–F3059.

Shabana, Y.M., Noda, N., 2008. Numerical evaluation of the thermomechanical effective properties of a functionally graded material using the homogenization method. Int. J. Solids Struct. 45, 3494–3506.

Terada, K., Kurumatani, M., Ushida, T., Kikuchi, N., 2010. A method of two-scale thermo-mechanical analysis for porous solids with micro-scale heat transfer. Comput. Mech. 46, 269–285.

Vel, S.S., Goupee, A.J., 2010. Multiscale thermoelastic analysis of random heterogeneous materials: Part I: microstructure characterization and homogenization of material properties. Comput. Mater. Sci. 48, 22–38.

Wan, T.H., Ciucci, F., 2017. Continuum level transport and electro-chemo-mechanics coupling—solid oxide fuel cells and lithium ion batteries. In: Electro-Chemo-Mechanics of Solids. Springer, pp. 161–189.

Wu, B., Lu, W., 2016. Mechanical-electrochemical modeling of agglomerate particles in lithium-ion battery electrodes. J. Electrochem. Soc. 163, A3131–A3139.

Wu, B., Lu, W., 2017. Mechanical modeling of particles with active core-shell structures for lithium-ion battery electrodes. J. Phys. Chem. C 121, 19022–19030.

Xu, R., de Vasconcelos, L.S., Zhao, K.J., 2016. Computational analysis of chemomechanical behaviors of composite electrodes in Li-ion batteries. J. Mater. Res. 31, 2715–2727.

Xu, R., Zhao, K.J., 2016. Mechanical interactions regulated kinetics and morphology of composite electrodes in Li-ion batteries. Extreme Mech. Lett. 8, 13–21.

Zhang, Q., Guo, Q.Z., White, R.E., 2006. A new kinetic equation for intercalation electrodes. J. Electrochem. Soc. 153, A301–A309.

Zhang, X., Shyy, W., Marie Sastry, A., 2007. Numerical simulation of intercalation-induced stress in li-ion battery electrode particles. J. Electrochem. Soc. 154, A910–A916.

Zhao, K.J., Pharr, M., Vlassak, J.J., Suo, Z.G., 2010. Fracture of electrodes in lithium-ion batteries caused by fast charging. J. Appl. Phys. 108 Article no. 073517.

Zhao, K.J., Pharr, M., Vlassak, J.J., Suo, Z.G., 2011. Inelastic hosts as electrodes for high-capacity lithium-ion batteries. J. Appl. Phys. 109 Article no. 016110.

Zhao, K.J., Pharr, M., Wan, Q., Wang, W.L., Kaxiras, E., Vlassak, J.J., Suo, Z.G., 2012. Concurrent reaction and plasticity during initial lithiation of crystalline silicon in lithium-ion batteries. J. Electrochem. Soc. 159, A238–A243.